Editors' Suggestion

Metastable skyrmion lattices governed by magnetic disorder and anisotropy in β-Mn-type chiral magnets

K. Karube,[1,*] J. S. White,[2,*] V. Ukleev,[2] C. D. Dewhurst,[3] R. Cubitt,[3] A. Kikkawa,[1] Y. Tokunaga,[4] H. M. Rønnow,[5] Y. Tokura,[1,6] and Y. Taguchi[1]

[1]*RIKEN Center for Emergent Matter Science (CEMS), Wako 351-0198, Japan*

[2]*Laboratory for Neutron Scattering and Imaging (LNS), Paul Scherrer Institute (PSI), CH-5232 Villigen, Switzerland*

[3]*Institut Laue-Langevin (ILL), 71 avenue des Martyrs, CS 20156, 38042 Grenoble cedex 9, France*

[4]*Department of Advanced Materials Science, University of Tokyo, Kashiwa 277-8561, Japan*

[5]*Laboratory for Quantum Magnetism (LQM), Institute of Physics, École Polytechnique Fédérale de Lausanne (EPFL), CH-1015 Lausanne, Switzerland*

[6]*Tokyo College and Department of Applied Physics, University of Tokyo, Bunkyo-ku 113-8656, Japan*

(Received 13 April 2020; accepted 23 July 2020; published 11 August 2020)

Magnetic skyrmions are vortexlike topological spin textures often observed in structurally chiral magnets with Dzyaloshinskii-Moriya interaction. Among them, Co-Zn-Mn alloys with a β-Mn-type chiral structure host skyrmions above room temperature. In this system, it has recently been found that skyrmions persist over a wide temperature and magnetic field region as a long-lived metastable state, and that the skyrmion lattice transforms from a triangular lattice to a square one. To obtain perspective on chiral magnetism in Co-Zn-Mn alloys and clarify how various properties related to the skyrmion vary with the composition, we performed systematic studies on $Co_{10}Zn_{10}$, $Co_9Zn_9Mn_2$, $Co_8Zn_8Mn_4$, and $Co_7Zn_7Mn_6$ in terms of magnetic susceptibility and small-angle neutron scattering measurements. Robust metastable skyrmions with extremely long lifetime are commonly observed in all the compounds. On the other hand, the preferred orientation of the helimagnetic propagation vector and its temperature dependence dramatically change upon varying the Mn concentration. The robustness of the metastable skyrmions in these materials is attributed to topological nature of the skyrmions as affected by structural and magnetic disorder. Magnetocrystalline anisotropy as well as magnetic disorder due to frustrated Mn spins play crucial roles in giving rise to the observed change in helical states and corresponding skyrmion lattice form.

DOI: 10.1103/PhysRevB.102.064408

I. INTRODUCTION

Noncollinear and noncoplanar spin textures have recently attracted much attention as a source of various emergent electromagnetic phenomena. Magnetic skyrmions, vortexlike spin textures characterized by an integer topological charge, are a prototypical example of such noncoplanar magnetic structures [1–4], and are anticipated to be applied to spintronics devices since they can be treated as particles and driven by an ultralow current density [5–7]. Thus far, skyrmions have been observed in various magnets due to several microscopic mechanisms, such as competition between the Dzyaloshinskii-Moriya interaction (DMI) and ferromagnetic exchange interaction [3,4,8–19], magnetic dipole interaction [20–23], and magnetic frustration or Ruderman-Kittel-Kasuya-Yosida (RKKY) interaction [24–26]. Among them, the DMI arises from the relativistic spin-orbit interaction in the presence of broken inversion symmetry either at interfaces of thin-film layers [8–12] or in bulk materials with noncentrosymmetric crystal structures [3,4,13–19].

In the structurally chiral magnets as represented by $B20$-type compounds (e.g., MnSi [3], $Fe_{1-x}Co_xSi$ [4], FeGe [13]) and Cu_2OSeO_3 [14] with the space group of $P2_13$, the DMI gradually twists ferromagnetically coupled moments to form a long-period helimagnetic state described by a magnetic propagation vector ($\boldsymbol{q}$ vector). The magnitude of $\boldsymbol{q}$ is given by $q \propto D/J$, where D and J correspond to the DMI constant and the exchange interaction, respectively, and the propagation direction is determined by magnetic anisotropy. Near the helimagnetic transition temperature T_c, magnetic fields induce a triangular-lattice skyrmion crystal (SkX) as illustrated in Fig. 1(c), which is often described as a triple-$\boldsymbol{q}$ structure with the $\boldsymbol{q}$ vectors displaying mutual 120° angles perpendicular to the magnetic field. In general, the SkX is stabilized by thermal fluctuations and thus its thermodynamic equilibrium state is confined to a narrow temperature and magnetic field region just below T_c, and topologically trivial helical or conical states are the thermodynamically most stable states at lower temperatures.

Recently, Co-Zn-Mn alloys have been identified as a new class of chiral magnets based on bulk DMI which host skyrmions above room temperature [15]. The materials crystallize in a β-Mn-type chiral cubic structure with the space group of $P4_132$ (defined as right-handed structure) or $P4_332$

*These authors contributed equally to this work.

 ©2020 American Physical Society

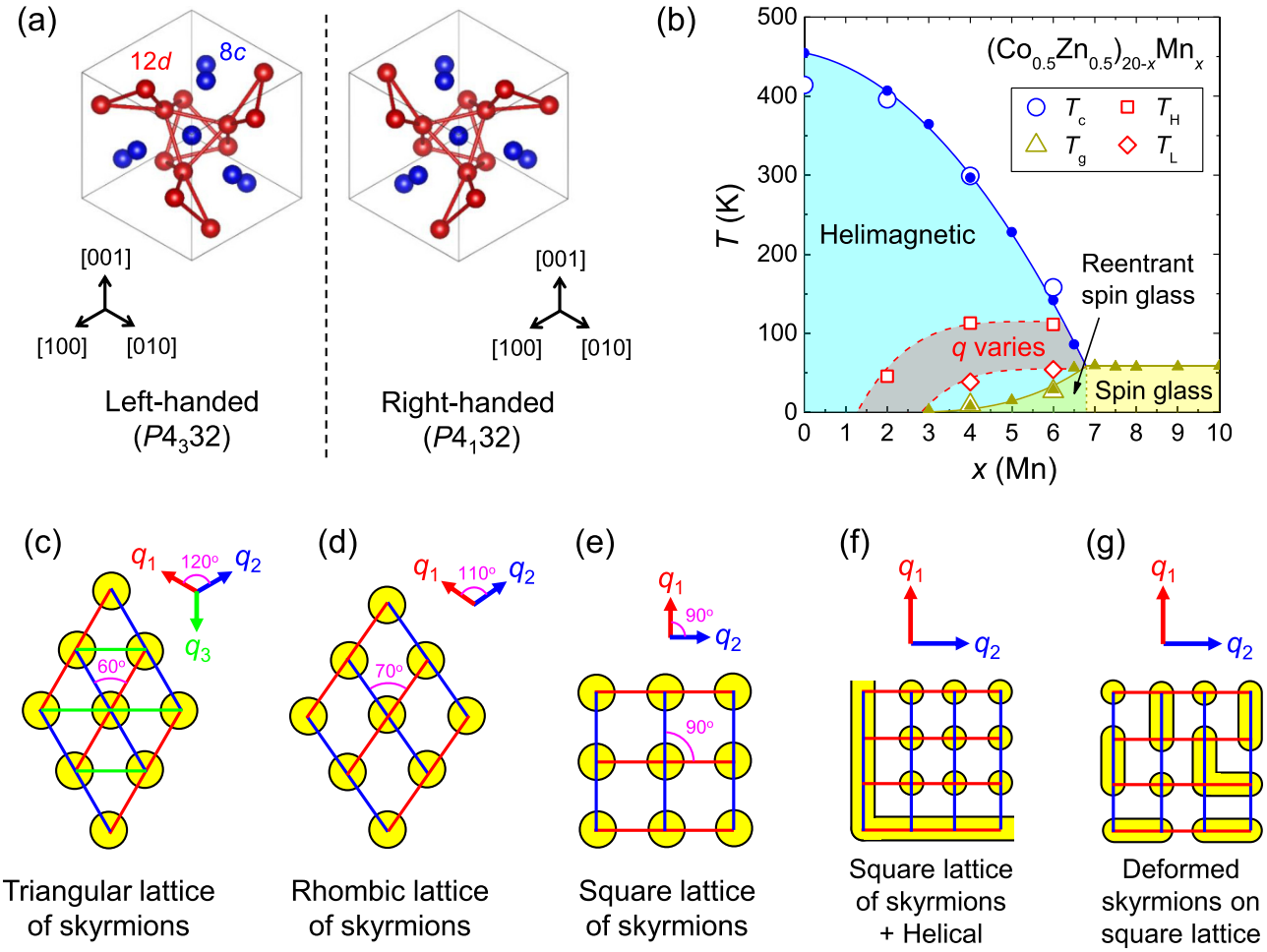

FIG. 1. (a) Schematics of β-Mn-type chiral crystal structures as viewed along the [111] direction. Two enantiomers with the space group $P4_332$ (left-handed structure) and $P4_132$ (right-handed structure) are shown. Blue and red circles represent 8*c* and 12*d* Wyckoff sites, respectively. The network of 12*d* sites forms a hyperkagome structure composed of corner-sharing triangles. (b) Temperature- (T-) Mn concentration (x) phase diagram in $(Co_{0.5}Zn_{0.5})_{20-x}Mn_x$ ($0 \leqslant x \leqslant 10$) at zero field, determined by magnetization (M) measurements. Closed symbols are data of polycrystalline samples reproduced from our previous work in Ref. [31] (Copyright 2018, American Association for the Advancement of Science). Open symbols are data of single-crystalline samples ($x = 0, 2, 4, 6$) in this study [see Figs. 3(a)–3(d) for the detailed determination of the phase boundaries]. A shaded region with red indicates the temperature range $T_L \leqslant T \leqslant T_H$ where M at 20 Oe and the magnitude of helical wave vector (q) vary (decreases and increases, respectively, on cooling) significantly. (c)–(g) Schematic illustrations of various skyrmion lattices: (c) triangular lattice, (d) rhombic lattice, (e) square lattice, (f) coexistence of square lattice of skyrmions and helical state, (g) I- or L-like deformed skyrmions on a square lattice. Corresponding hybridized $\boldsymbol{q}$ vectors are also presented in each panel.

(left-handed structure), where 20 atoms per unit cell are distributed over two Wyckoff sites (8*c* and 12*d*) as illustrated in Fig. 1(a). The 8*c* sites are mainly occupied by Co atoms while the 12*d* sites are mainly occupied by Zn and Mn [27–30]. The β-Mn-type structure forms in all the solid solutions of $(Co_{0.5}Zn_{0.5})_{20-x}Mn_x$ from $Co_{10}Zn_{10}$ to Mn_{20} (β-Mn itself) [27,31].

The magnetic phase diagram on the plane of temperature (T) and Mn concentration (x) is reproduced from Ref. [31] and displayed in Fig. 1(b) with additional information obtained in this study. One end member $Co_{10}Zn_{10}$ shows a helimagnetic ground state with Ref. [15] reporting a magnetic periodicity $\lambda \sim 185$ nm below $T_c \sim 460$ K. T_c rapidly decreases as partial substitution of Mn proceeds, and $Co_8Zn_8Mn_4$ with $T_c \sim 300$ K exhibits a thermally equilibrium SkX state at room temperature under magnetic fields. The magnitude of the DMI constant in $Co_8Zn_8Mn_4$ has been experimentally evaluated to be $D \sim 0.53$ mJ/m^2, which is several times smaller than that in FeGe [32]. The DMI critically depends on the band structure and electron band filling as demonstrated in Fe-doped $Co_8Zn_8Mn_4$, where even a sign change in the DMI, namely, reversal of skyrmion helicity, occurs as the Fe concentration is increased [33].

Although the thermodynamic equilibrium SkX phase in $Co_8Zn_8Mn_4$ exists only in a narrow temperature and magnetic field region, it has been demonstrated that a once-created SkX can persist over the whole temperature region below room temperature and a wide magnetic field region as a long-lived metastable state via a conventional (a few K/min) field cooling (FC) [34]. Moreover, the lattice form of the metastable SkX undergoes a reversible transition, accompanied by large increase in q, from a conventional triangular lattice to a novel square one, which is described as an orthogonal double-q state, as illustrated in Fig. 1(e) [35]. A similar

robust metastable SkX has been observed in $Co_9Zn_9Mn_2$ with $T_c \sim 400$ K, where the metastable SkX persists even at zero field above room temperature [36]. By means of Lorentz transmission electron microscopy (LTEM) for thin-plate specimens, various exotic skyrmion-related structures, such as I- or L-shaped elongated skyrmions [37] [Fig. 1(g)], a smectic liquid-crystalline structure of skyrmions [38] and a meron-antimeron square lattice [39], have been observed.

The other end member β-Mn is well known as a spin liquid, while the lightly doped β-Mn alloys with slight disorder exhibit a spin glass, due to geometrical frustration among antiferromagnetically coupled Mn spins in the hyperkagome network of the 12*d* sites [40–45]. Therefore, $(Co_{0.5}Zn_{0.5})_{20-x}Mn_x$ possesses both magnetic frustration inherent to β-Mn and magnetic disorder due to the mixture of ferromagnetic Co spins and antiferromagnetic Mn spins, which give rise to a spin-glass phase below T_g over a wide range of the Mn concentration ($3 \leqslant x \leqslant 19$) [31]. In particular, the spin-glass phase invades the helical phase for $3 \leqslant x \leqslant 7$ displaying reentrant spin-glass behavior [46] as similarly reported for a number of ferromagnets [47–52], antiferromagnets [53,54], and helimagnets [55] with chemical and magnetic disorder. The spin-glass nature was confirmed by previous frequency-dependent ac susceptibility measurements for $Co_7Zn_7Mn_6$ ($T_c \sim 160$ K, $T_g \sim 30$ K) [29,31,56]. It has been discovered that a novel equilibrium phase of disordered skyrmions exists just above T_g in $Co_7Zn_7Mn_6$, which is thermodynamically disconnected from the conventional equilibrium SkX phase just below T_c, and presumably stabilized by a cooperative interplay between the chiral magnetism with DMI and the frustrated magnetism [31].

Despite these extensive studies for Co-Zn-Mn alloys, it remains elusive how the (meta)stability and lattice form of skyrmions vary with the Mn concentration from the end member $Co_{10}Zn_{10}$, and how the two magnetic elements of Co and Mn contribute to the skyrmion formation and the transformation of the skyrmion lattice. In order to obtain a more complete perspective on the skyrmion states in the Co-Zn-Mn alloys, here we present data sets obtained by small-angle neutron scattering (SANS) and magnetic susceptibility that have not been reported previously. From the data we report the following: (i) identification of the equilibrium skyrmion phase, and temperature and field dependence of helical and metastable skyrmion states in $Co_{10}Zn_{10}$, (ii) an off-axis magnetic field experiment for metastable skyrmions in $Co_8Zn_8Mn_4$ to reveal the role of anisotropy, (iii) temperature and field dependence of metastable skyrmions in $Co_9Zn_9Mn_2$ below ambient temperature down to the lowest temperature to clarify the effect of dilute Mn moments that becomes significant only at low temperatures, (iv) temperature and field evolution of heavily disordered metastable skyrmions in $Co_7Zn_7Mn_6$, and (v) lifetime of metastable skyrmions in $Co_{10}Zn_{10}$ and $Co_8Zn_8Mn_4$. Combining these results together with our previous ones, we show systematic changes in lattice forms and lifetimes of the metastable skyrmions, as well as the key roles of magnetic disorder and anisotropy, as functions of temperature and Mn concentration. As summarized in Fig. 2, the metastable skyrmion state prevails in a wide temperature and field range for all

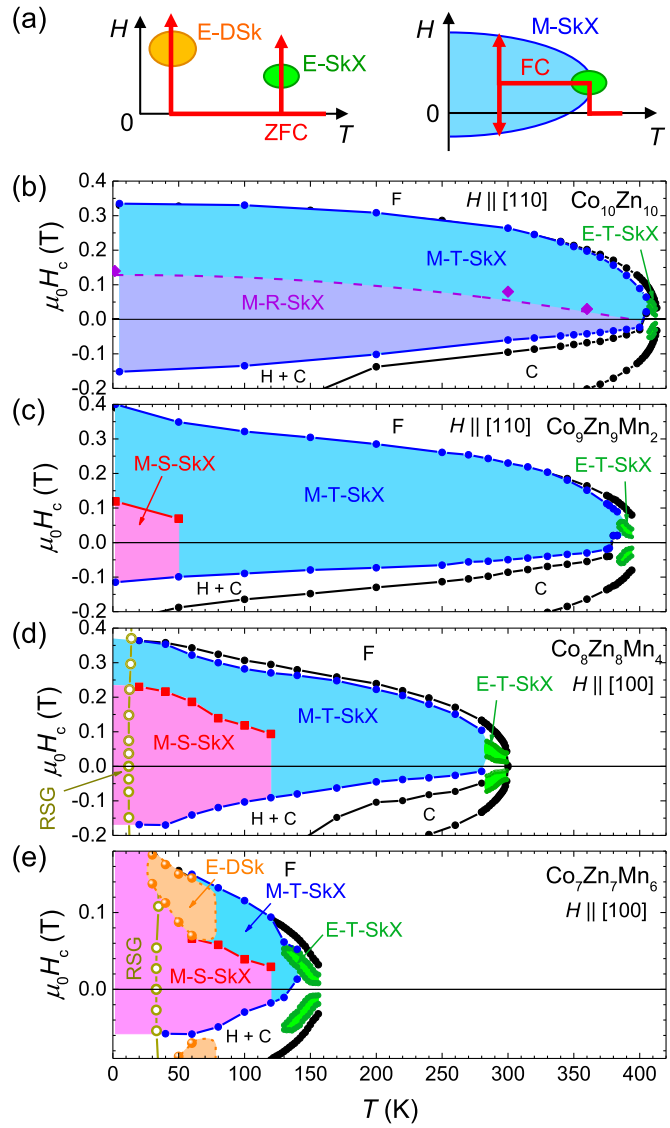

FIG. 2. Summary of equilibrium and metastable skyrmion states in the temperature–magnetic field (T-H) plane in (b) $Co_{10}Zn_{10}$, (c) $Co_9Zn_9Mn_2$, (d) $Co_8Zn_8Mn_4$ (reproduced from our previous work in Ref. [34], Copyright 2016, Springer Nature), and (e) $Co_7Zn_7Mn_6$. The measurement processes for the state diagrams are schematically illustrated in (a). The equilibrium skyrmion crystal (SkX) phase just below T_c (green area) and the equilibrium disordered skyrmion (DSk) phase (orange area) are determined by field-sweeping measurements of ac susceptibility and SANS after zero-field cooling (ZFC). The metastable SkX state [triangular lattice (light blue area), rhombic lattice (purple area), and square lattice (pink area)] are determined by field-sweeping measurements toward positive and negative directions after field cooling (FC) via the positive-field equilibrium SkX phase. Here, we use the following notations: H, helical; C, conical; F, ferromagnetic; E, equilibrium; M, metastable; T, triangular; R, rhombic; S, square; SkX, skyrmion crystal; DSk, disordered skyrmions; and RSG, reentrant spin glass. The phase boundaries are determined by ac susceptibility (χ'). For the purpose of comparison with SANS measurements, calibrated values (H_c) are used for the magnetic field. The details about the determination of the phase boundaries of the equilibrium SkX state and the metastable SkX state in $Co_{10}Zn_{10}$ are described in the captions of Fig. 4(d) and Supplemental Material [57], Fig. S2(c),

the materials. In $Co_{10}Zn_{10}$, triangular lattice of skyrmions transforms to rhombic-like [Fig. 1(d)] as the temperature is lowered in a low field. This triangular-rhombic structural transformation is governed by enhanced magnetocrystalline anisotropy that favors $\boldsymbol{q} \parallel \langle 111 \rangle$. On the other hand, in the Mn-doped compounds, the $\boldsymbol{q}$-vector orientation changes from $\langle 111 \rangle$ to $\langle 100 \rangle$, and a structural transformation from triangular lattice to square one occurs at low temperatures and low fields. As the Mn concentration is increased, and as the helimagnetic T_c thus falls, antiferromagnetic correlations of Mn spins start to develop on cooling from higher temperatures. The resulting magnetic disorder drives a large increase in q value, thereby triggering the transformation to the square-lattice state, in cooperation with the enhanced magnetic anisotropy toward $\boldsymbol{q} \parallel \langle 100 \rangle$ at low temperatures.

The format of this paper is as follows. After we describe experimental methods in Sec. II, results and discussion are presented in Sec. III, and conclusion is given in Sec. IV. In Sec. III, we first overview helical and skyrmion states in all the compounds (Sec. III A, Figs. 2 and 3, Table I). Then, we show detailed results of magnetic susceptibility and SANS measurements for each composition: $Co_{10}Zn_{10}$ (Sec. III B, Figs. 4–6), $Co_8Zn_8Mn_4$ (Sec. III C, Fig. 7), $Co_9Zn_9Mn_2$ (Sec. III D, Fig. 8), and $Co_7Zn_7Mn_6$ (Sec. III E, Figs. 9–11), and summarize all of them (Sec. III F). Finally, we present the composition dependence of the lifetime of metastable skyrmions (Sec. III G, Figs. 12 and 13). Armed with all these results, we discuss the roles of magnetic disorder and anisotropy in leading to the robust metastable skyrmions and their novel lattice forms in Co-Zn-Mn alloys.

II. EXPERIMENTAL METHODS

A. Sample preparation

Single-crystalline $Co_{10}Zn_{10}$ was grown by a self-flux method in an evacuated quartz tube. The single crystals were cut along the (110), (−110), and (001) planes with rectangular shapes for magnetization and ac susceptibility measurements, as well as SANS measurement after the crystalline orientation was determined by the x-ray Laue diffraction method. Single crystals of $Co_9Zn_9Mn_2$, $Co_8Zn_8Mn_4$, and $Co_7Zn_7Mn_6$ were grown by the Bridgman method as described in our previous papers [31,34,36], and were cut along the (110), (−110), and (001) planes for $Co_9Zn_9Mn_2$, and along the (100), (010), and (001) planes for each of $Co_8Zn_8Mn_4$ and $Co_7Zn_7Mn_6$.

B. Magnetization and ac susceptibility measurements

Magnetization and ac susceptibility measurements were performed with a superconducting quantum interference device magnetometer (MPMS3, Quantum Design). High-temperature measurements above 400 K for $Co_{10}Zn_{10}$ were performed using an oven option. In the ac susceptibility measurements, the ac drive field was set as $H_{ac} = 1$ Oe for all the compounds, and the ac frequency was selected to be $f = 17$ Hz for $Co_{10}Zn_{10}$ and $f = 193$ Hz for $Co_9Zn_9Mn_2$, $Co_8Zn_8Mn_4$, and $Co_7Zn_7Mn_6$. Magnetic fields were applied along the [110] direction for $Co_{10}Zn_{10}$ and $Co_9Zn_9Mn_2$, and along the [100] direction for $Co_8Zn_8Mn_4$ and $Co_7Zn_7Mn_6$, respectively. Due to the difference in the shape between the samples used in the ac susceptibility (field parallel to the plate) and the SANS measurements (field perpendicular to the plate), their demagnetization factors are different. To correct for this difference so that a common absolute magnetic field scale is used throughout this paper, the field values for the ac susceptibility measurements are calibrated as $H_c = NH$ where $N = 3.0$, 2.0, 3.7, and 2.7 for $Co_{10}Zn_{10}$, $Co_9Zn_9Mn_2$, $Co_8Zn_8Mn_4$, and $Co_7Zn_7Mn_6$, respectively.

C. Small-angle neutron scattering (SANS) measurements

SANS measurements for $Co_{10}Zn_{10}$, $Co_9Zn_9Mn_2$, and $Co_8Zn_8Mn_4$ were performed using the SANS-I instrument at the Paul Scherrer Institute (PSI), Switzerland. For high-temperature measurements above 300 K for $Co_{10}Zn_{10}$ and $Co_9Zn_9Mn_2$, a bespoke oven stick designed for SANS experiments was used. SANS measurements of $Co_7Zn_7Mn_6$ were done using the D33 instrument at the Institut Laue-Langevin (ILL), France. The neutron wavelength was selected to be 10 Å with a 10% full width at half-maximum (FWHM) spread in all the measurements. For all the SANS data shown here, nuclear and instrumental background signals have been subtracted by using data taken either well above the helimagnetic ordering temperature T_c, or well above the polarized ferromagnetic transition field.

For $Co_{10}Zn_{10}$, the mounted single-crystalline sample was installed into a horizontal field cryomagnet so that the incident neutron beam (k_i) and the magnetic field (H) were parallel to the [110] direction. The cryomagnet was rotated ("rocked") together with the sample around the vertical [001] direction, and the rocking angle (ω) between k_i and H was scanned from −20° to 20° by 2° step. Here, $\omega = 0°$ corresponds to the $k_i \parallel H$ configuration. The observed FWHM of the rocking curves (scattering intensity versus ω) was always broader than 19°. Therefore, to deduce accurately the relative intensities and positions of all of the Bragg spots in single images, all the SANS images displayed in this paper are obtained by summing multiple SANS measurements taken over $-8° \leqslant \omega \leqslant 8°$.

As detailed in our previous papers [31,34,36], similar SANS measurements were performed with the $k_i \parallel H \parallel [110]$ configuration for $Co_9Zn_9Mn_2$, and $k_i \parallel H \parallel [001]$ configuration for $Co_8Zn_8Mn_4$ and $Co_7Zn_7Mn_6$.

respectively. The boundaries between the metastable triangular SkX and the metastable rhombic SkX (purple diamonds) are determined from SANS results [see Fig. 6(d) and Supplemental Material [57], Figs. S2(d) and S3(d), for the details]. The boundary between the metastable triangular SkX and the metastable square SkX (red squares) are determined as inflection points of $\chi'(H)$ as detailed in Ref. [34]. The reentrant spin-glass transition temperatures (yellow open circles) are determined as inflection points of a sharp drop in $\chi'(T)$, as also observed in $M(T)$ in the zero-field-cooled field-warming process [Figs. 3(c) and 3(d)]. The equilibrium DSk phase in $Co_7Zn_7Mn_6$, determined as the region where a spherical SANS pattern is observed, is reproduced from our previous work in Ref. [31] (Copyright 2018, American Association for the Advancement of Science).

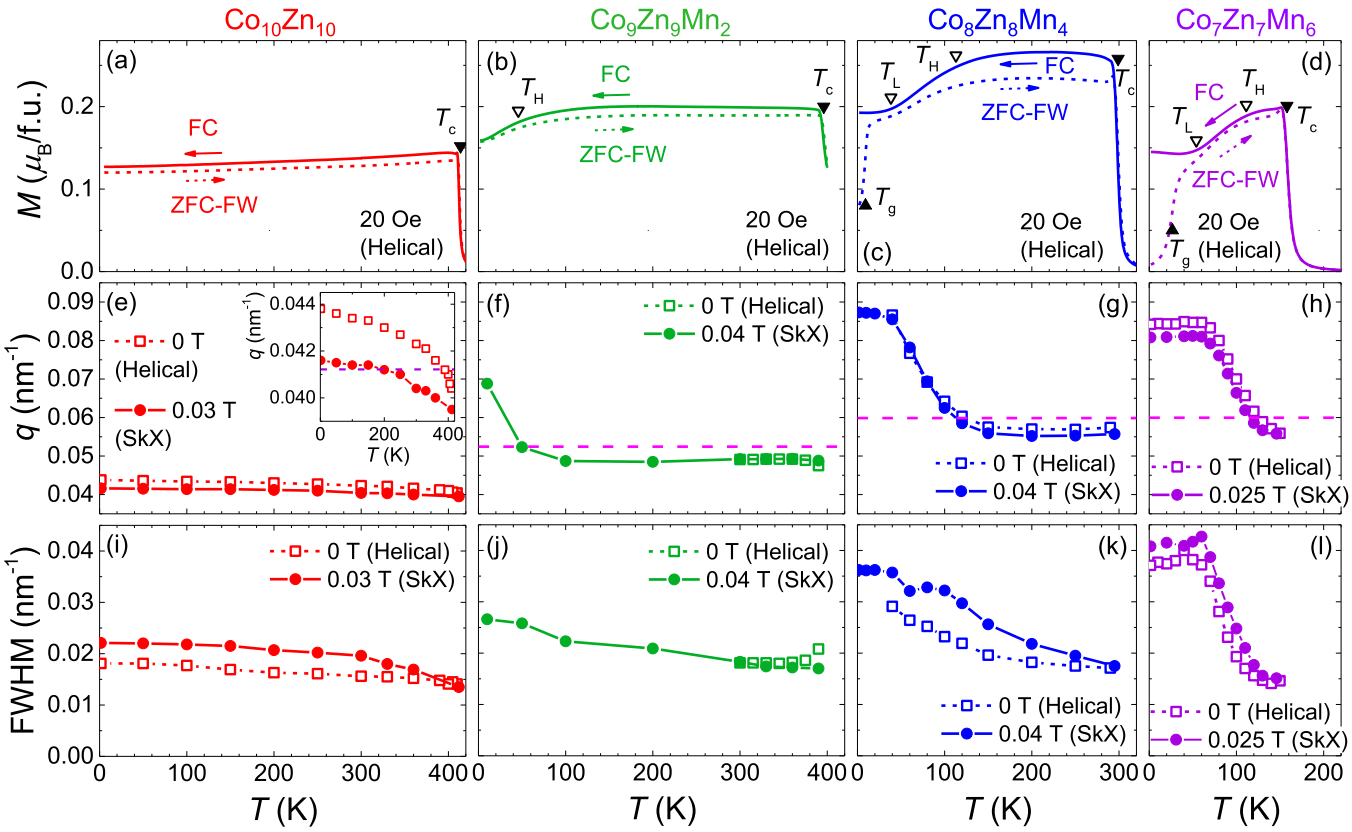

FIG. 3. Temperature dependence of the magnetization and $\boldsymbol{q}$ vector in $Co_{10}Zn_{10}$ (red), $Co_9Zn_9Mn_2$ (green), $Co_8Zn_8Mn_4$ (blue), and $Co_7Zn_7Mn_6$ (purple). (a)–(d) Magnetization (M) under a magnetic field of 20 Oe is plotted against temperature. Solid lines show the data collected during field cooling (FC), and broken lines represent those taken in a field-warming run after a zero-field cooling down to 2 K (ZFC-FW). The helimagnetic transition temperature (T_c) indicated with closed triangles is determined as an inflection point due to a sharp increase in M on the FC process. T_H and T_L are the temperatures at which a gradual decrease in M on cooling starts and ends, respectively. These temperatures are determined as inflection points with a broad peak in dM/dT on the FC process and indicated by open triangles. The reentrant spin-glass transition temperature (T_g) denoted with closed triangles is determined as an inflection point of a sharp increase in M on the ZFC-FW process. These temperatures are also plotted in the T-x phase diagram in Fig. 1(b). (e)–(h) Temperature variation of the magnitude of q in the helical state at zero field (open squares), and q in equilibrium and metastable SkX states under magnetic fields (closed circles). The q values are determined as the peak center of Gaussian function fitted to the SANS intensity as a function of q. The inset of (e) shows an enlarged view of $q(T)$ for $Co_{10}Zn_{10}$. The purple dashed line in the inset of (e) and the pink dashed line in (f)–(h) indicate the expected q values for rhombic and square lattice of skyrmions ($=1.043q_T$ and $1.075q_T$, where q_T are the values in the equilibrium triangular SkX state), respectively, with the assumption of constant skyrmion density from the high-temperature triangular lattice (see discussion in Sec. III F 2 for the details). (i)–(l) Temperature dependence of full width at half-maximum (FWHM) of the Gaussian function fitted to the SANS intensity versus q curves.

III. RESULTS AND DISCUSSION

A. Overview of state diagrams

First, we briefly overview the results of the basic magnetic properties in helimagnetic and metastable skyrmion states for all the compounds.

1. Helical state

Figures 3(a)–(d) show the temperature (T) dependence of the magnetization (M) under a small magnetic field of 20 Oe. In $Co_{10}Zn_{10}$, M shows a sharp increase due to a helimagnetic transition at $T_c \sim 414$ K, and then stays almost independent of temperature both for the field-cooling (FC) and the zero-field-cooled field-warming (ZFC-FW) processes. The other compounds exhibit a gradual decrease in M upon cooling through some temperature region ($T_L \leqslant T \leqslant T_H$). $Co_9Zn_9Mn_2$ shows an almost temperature-independent M over a wide temperature range below $T_c \sim 396$ K, while the gradual decrease is observed below $T_H \sim 50$ K. In $Co_8Zn_8Mn_4$, the T-independent behavior below $T_c \sim 299$ K is followed by the gradual decrease in M upon cooling from $T_H \sim 120$ K down to $T_L \sim 40$ K. A sharp drop of M at $T_g \sim 9$ K observed only in the ZFC-FW process is due to a reentrant spin-glass transition. $Co_7Zn_7Mn_6$ exhibits the gradual decrease in M below $T_H \sim 120$ K down to $T_L \sim 50$ K below the helimagnetic transition at $T_c \sim 158$ K. The reentrant spin-glass transition is observed around $T_g \sim 26$ K as manifested in the large deviation between FC and ZFC-FW processes. The reentrant spin-glass transition temperature T_g determined by the $M(T)$ curve is very close to the zero-frequency limit of T_g determined by ac susceptibility data obtained at various frequencies as previously reported [56]. T_g does not show a significant dependence on the magnetic field below the field-

TABLE I. Summary of several physical parameters describing the helimagnetic state in $Co_{10}Zn_{10}$, $Co_9Zn_9Mn_2$, $Co_8Zn_8Mn_4$, and $Co_7Zn_7Mn_6$. Helimagnetic transition temperature T_c is determined from the temperature variation in magnetization under 20 Oe. Saturation magnetization M_s is defined as a magnetization value at 2 K and 7 T. Helimagnetic periodicities λ (maximum value λ_{max} at high temperature and minimum value λ_{min} at low temperature) are calculated from the q values obtained from SANS measurements in zero field. The preferred orientation of the helical $\boldsymbol{q}$ vector is also determined from SANS measurements.

Composition	$Co_{10}Zn_{10}$	$Co_9Zn_9Mn_2$	$Co_8Zn_8Mn_4$	$Co_7Zn_7Mn_6$
T_c (K)	414	396	299	158
M_s (μ_B/f.u.)	11.3	14.3	12.7	7.97
λ_{max} (nm)	156	132	110	112
λ_{min} (nm)	143	91	73	74
Preferred $\boldsymbol{q}$ direction	$\langle 111\rangle$	$\langle 100\rangle$	$\langle 100\rangle$	$\langle 100\rangle$

induced ferromagnetic region as plotted in the phase diagrams show in Figs. 2(d) and 2(e). These characteristic temperatures (T_c, T_H, T_L, and T_g) are plotted in the T-x phase diagram in Fig. 1(b).

Magnetization curves at 2 K that characterize the ground states are shown in the Supplemental Material, Fig. S1 [57]. The values of T_c and saturation magnetization M_s at 2 K and at 7 T in all the compounds are summarized in Table I. From the value of $M_s \sim 11.3\mu_B$/f.u. in $Co_{10}Zn_{10}$, the magnetic moment at Co site is estimated to be $\sim 1.1\mu_B$. While T_c monotonically decreases with increasing Mn concentration, M_s displays a maximum in $Co_9Zn_9Mn_2$.

The characteristic T dependence of M at 20 Oe is compared with that of the magnitude of helical wave vector (q) from SANS measurements in Figs. 3(e)–3(h). It turns out that the gradual decrease in M from T_H to T_L corresponds to a large increase in the value of q, i.e., decrease in the helimagnetic periodicity λ ($=2\pi/q$). The largest value of λ at high temperatures (λ_{max}) and the smallest value of λ at low temperatures (λ_{min}) for each compound are summarized in Table I. We also present the preferred orientation of $\boldsymbol{q}$ in Table I. While the preferred $\boldsymbol{q}$ direction is $\langle 111\rangle$ for $Co_{10}Zn_{10}$, it is parallel to $\langle 100\rangle$ in $Co_9Zn_9Mn_2$, $Co_8Zn_8Mn_4$, and $Co_7Zn_7Mn_6$, as detailed in the following sections.

2. Metastable skyrmion state

Figure 2 shows the T-H diagrams determined by ac susceptibility and SANS measurements for each composition. In these diagrams, the equilibrium SkX phase and the metastable SkX state are presented together, as determined by field scans after ZFC and by field scans after a FC via the equilibrium phase, respectively, as schematically illustrated in Fig. 2(a). The robust metastable skyrmion state that exists over a very wide temperature and field region is commonly observed from $Co_{10}Zn_{10}$ to $Co_7Zn_7Mn_6$. In $Co_{10}Zn_{10}$ the triangular lattice of metastable skyrmions (M-T-SkX) distorts and transforms to a rhombic one (M-R-SkX) at low fields during the FC. On the other hand, the lattice form changes to a square one (M-S-SkX) at low temperatures and low fields in the other Mn-doped compounds. As partial Mn substitution proceeds, the phase space of the metastable triangular SkX state (M-T-SkX) is squeezed, accompanied by the suppression of T_c, while the region occupied by square SkX state (M-S-SkX) expands toward higher temperatures. The transition to the square SkX is accompanied by a large increase in q as observed similarly in the helical states [Figs. 3(f)–3(h)].

B. $Co_{10}Zn_{10}$

In this section, we present detailed results of SANS and ac susceptibility measurements for $Co_{10}Zn_{10}$, show that the preferred orientation of $\boldsymbol{q}$ vector is $\langle 111\rangle$ direction, and that on field-cooling the metastable skyrmion lattice distorts and undergoes a structural transformation from a conventional triangular lattice to a rhombic one.

1. Identification of equilibrium SkX

First, we identify equilibrium SkX phases (Fig. 4). Photographs of single-crystalline samples used for SANS and ac susceptibility measurements are shown in Fig. 4(a). Figure 4(b) shows the field variation of SANS images at 410 K. The scattering signal observed at 0 T is attributed to a helical multidomain state. Here, four broad spots are observed but the peak positions are not aligned clearly to any unique set of high-symmetry crystal axes. This peculiar scattering distribution near T_c may be attributed to a rather flexible nature of the $\boldsymbol{q}$ vector due to the negligible anisotropy at high temperatures under an influence of possible residual local strain of the sample. Under magnetic fields parallel to the incident neutron beam, the SANS signal diminishes at 0.02 T most likely due to the transition to the conical state whose $\boldsymbol{q}$ vector is parallel to the field and thus not detected in this configuration. At 0.03 T, a broad six-spot pattern, a hallmark of a triangular lattice of skyrmions (triple-$\boldsymbol{q} \perp H$) appears. As the magnetic field is further increased to 0.06 T, the conical state is stabilized again and the signal disappears. The SANS intensity perpendicular to the field is plotted against field in Fig. 4(c). The SANS intensity exhibits a peak at 0.03 T, where the volume fraction of skyrmions is maximized.

The field dependence of the real (χ') and imaginary (χ'') parts of the ac susceptibility at 410 K is shown in Fig. 4(d). A dip structure is observed in χ' between 0.02 and 0.05 T where in addition χ'' exhibits a clear double-peak structure. These features correspond to a SkX phase surrounded by a conical phase, and show a good agreement with the region of the enhanced SANS intensity. Therefore, the phase boundaries of the SkX phase are determined as the peak positions at the both sides of the dip structure in χ'. Contour plots of χ' and χ'' with the phase boundaries on the T-H plane are presented in Figs. 4(e) and 4(f), respectively. The equilibrium SkX phase exists in a narrow temperature region from $T_c \sim 412$ K down

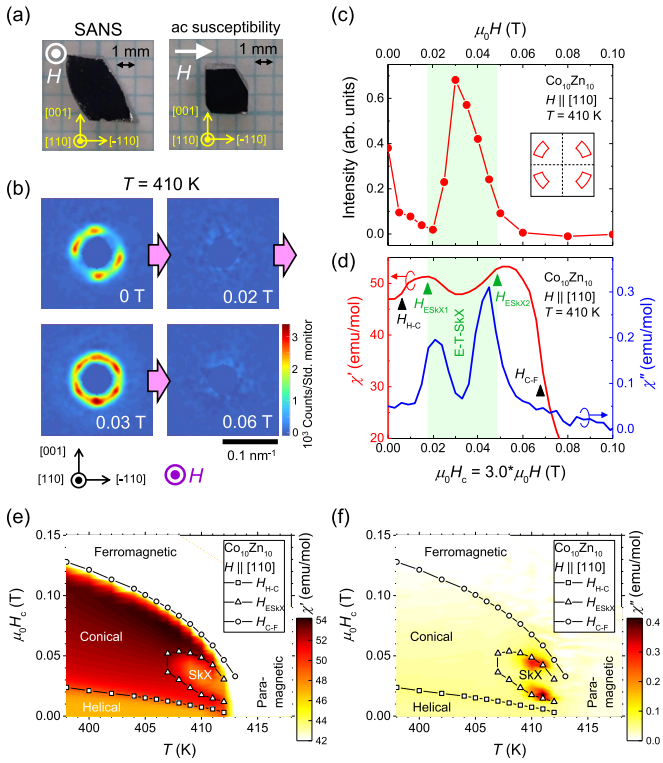

FIG. 4. Identification of the equilibrium SkX phase in $Co_{10}Zn_{10}$. (a) Photos of single-crystalline bulk samples of $Co_{10}Zn_{10}$ used for SANS and ac susceptibility measurements. Crystal axes and the direction of applied magnetic field (H) are also indicated. (b) SANS images at selected fields in the field increasing run at 410 K. The intensity scale of the color plot is fixed for the four panels. (c) Field dependence of SANS intensity at 410 K. The intensity was integrated over the region close to ⟨111⟩ (red areas in the inset) as detailed in Fig. 5(c). (d) Field dependence of the real part (χ', red line) and the imaginary part (χ'', blue line) of the ac susceptibility in the field increasing run at 410 K. Since the demagnetization factor is different from that in the SANS measurement, the field values are calibrated as $H_c = 3.0 \times H$. The phase boundary between the helical and conical states ($H_{H\text{-}C}$, black triangle) is determined as the inflection point of χ'. The phase boundaries between the equilibrium SkX and conical states ($H_{ESkX1(2)}$, green triangles) are determined as the peak positions at both sides of the dip structure in χ'. The phase boundary between the conical and induced-ferromagnetic states ($H_{C\text{-}F}$, black triangle) is determined as the inflection point of χ'. The equilibrium SkX region is indicated with the light green shading in (c) and (d). (e) Contour plot of χ' on the T-H_c plane. The region with $\chi' \leqslant 42$ emu/mol is displayed with white color. (f) Contour plot of χ'' on the T-H_c plane. Phase boundaries determined by χ' (d) and similar data points at different temperatures are plotted as open symbols in (e) and (f).

to 407 K, below which the field-induced conical phase is the most stable.

2. *Temperature evolution of helical state in zero field*

Next, we discuss the temperature variation of the helical state (Fig. 5). Figure 5(b) shows the SANS patterns at selected temperatures on zero-field cooling from 410 to 1.5 K. As temperature is lowered from T_c down to 300 K, the SANS intensity gradually accumulates along the [1−11] direction due to an enhancement of the magnetic anisotropy. Upon further

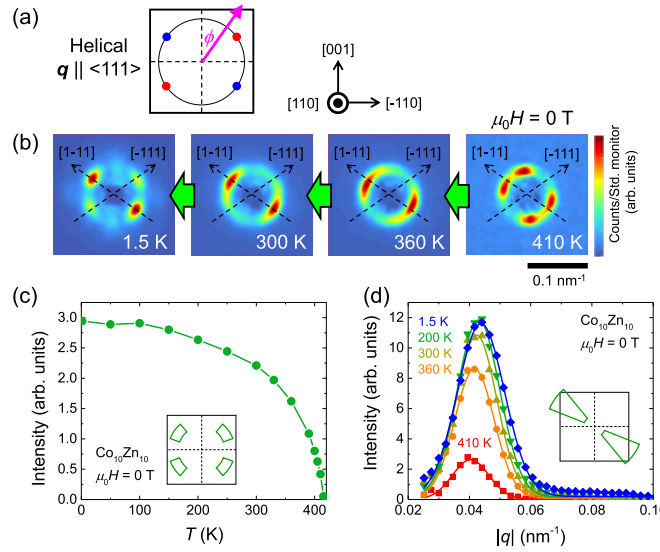

FIG. 5. Temperature dependence of the helical state in $Co_{10}Zn_{10}$ in zero field. (a) Schematic SANS pattern on the (110) plane expected for a helical state with $\boldsymbol{q} \parallel \langle 111 \rangle$. The helical state forms four domains with $\boldsymbol{q} \parallel [-111]$ (two red spots), $[1-11]$ (two blue spots), $[11-1]$ (out of the plane), and $[111]$ (out of the plane), respectively, resulting in four spots on the (110) plane at $\phi = 55°$, $125°$, $235°$, $305°$. Here, ϕ is defined as the clockwise azimuthal angle from the vertical direction. (b) SANS images observed at 410, 360, 300, and 1.5 K. The intensity scale of the color plot varies between each panel. The $[-111]$ and $[1-11]$ directions are indicated with broken arrows. (c) Temperature dependence of the SANS intensity integrated over the azimuthal angle area at $\phi = 55°$, $125°$, $235°$, $305°$ with the width of $\Delta\phi = 30°$ (green area in the inset). (d) Radial $|q|$ dependence of SANS intensity, integrated over the azimuthal angle area at $\phi = 125°$, $305°$ with the width of $\Delta\phi = 30°$ (green areas in the inset), at several temperatures. The data points are fitted to a Gaussian function (solid lines).

decreasing temperature down to 1.5 K, the SANS intensity splits into four spots: two spots with stronger intensity along the $[1-11]$ direction, and the other two spots with weaker intensity along the $[-111]$ direction. This four-spot pattern at 1.5 K is expected for the multidomain helical state with $\boldsymbol{q} \parallel \langle 111 \rangle$ as illustrated schematically in Fig. 5(a). Notably, the preferred orientation of the $\boldsymbol{q}$ vector in $Co_{10}Zn_{10}$ is different from those of the other $(Co_{0.5}Zn_{0.5})_{20-x}Mn_x$ systems with $x \geqslant 2$, which is found to be ⟨100⟩ in our previous studies [31,34,36].

Figure 5(c) shows the temperature dependence of the SANS intensity integrated for the $[-111]$ and $[1-11]$ directions ($\phi = 55°$, $125°$, $235°$, and $305°$), where a conventional order-parameter-like evolution of the intensity for $\boldsymbol{q} \parallel \langle 111 \rangle$ is clearly observed. The radial q dependence of the SANS intensity for the direction close to $[1-11]$ is displayed in Fig. 5(d). The peak center slightly shifts toward higher-q and the peak width slightly increases on cooling. The helical q value, which is determined as the peak center of a Gaussian function fitted to the intensity vs q curve [solid lines in Fig. 5(d)], and its FWHM are plotted against temperature in Figs. 3(e) and 3(i), respectively. Both the q value and the FWHM gradually increase on cooling but the variation is much smaller than that in the Mn-doped compounds. The

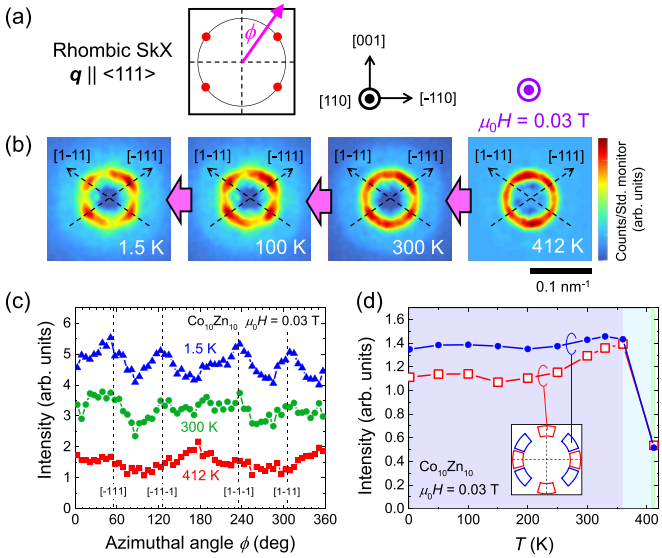

FIG. 6. Metastable SkX state in $Co_{10}Zn_{10}$ during a field-cooling process at 0.03 T. (a) Schematic SANS pattern on the (110) plane, perpendicular to the field, expected for a rhombic SkX with $\boldsymbol{q} \parallel \langle 111 \rangle$. (b) SANS images measured at 412, 300, 100, and 1.5 K during the FC process at 0.03 T. The intensity scale of the color plot varies between each panel. The magnetic field was applied at 412 K after ZFC. (c) Azimuthal angle (ϕ) dependence of SANS intensity at 412, 300, and 1.5 K. The intensity data for 1.5 K is vertically shifted by 2 for clarity. The angles corresponding to the [−111] and [1−11] directions ($\phi = 55°$, 125°, 235°, and 305°) are indicated by dashed lines. (d) Temperature dependence of the SANS intensity. Blue symbols denote the intensity integrated over the region close to the [−111] and [1−11] directions ($\phi = 55°$, 125°, 235°, and 305° with the width of $\Delta\phi = 30°$; blue areas in the inset). The intensity integrated over the region around the [001] and [−110] directions ($\phi = 0°$, 90°, 180°, and 270° with the width of $\Delta\phi = 30°$; red areas in the inset) are denoted by red symbols. The temperature regions of the equilibrium triangular SkX, metastable triangular SkX, and metastable rhombic SkX are indicated with the light green, light blue, and purple shadings, respectively.

helical periodicity estimated as $\lambda = 2\pi/q$ varies a little from 156 to 143 nm on cooling as summarized in Table I. Note that the values of $T_c = 414$ K and $\lambda = 156$ nm for a single crystal of $Co_{10}Zn_{10}$ in this study are smaller than the values ($T_c = 462$ K and $\lambda = 185$ nm) for a polycrystalline sample in the previous study [15], probably due to a slight difference in the composition.

As detailed in the Supplemental Material [57], Fig. S4, we also find that the helical state at 1.5 K forms a chiral soliton lattice [59] under magnetic fields due to the enhanced magnetocrystalline anisotropy which enforces the $\boldsymbol{q}$ vector along $\langle 111 \rangle$, and perpendicular to the field.

3. *Temperature dependence of metastable SkX*

Next, we discuss the temperature variation of the metastable SkX state (Fig. 6). The SANS patterns obtained during FC at 0.03 T from 412 to 1.5 K are displayed in Fig. 6(b). In order to gain a sufficient cooling rate across the boundary between the equilibrium SkX and conical phases, the magnetic field was applied at 412 K (slightly higher than presented in Fig. 4). At this temperature the observed SANS pattern is ringlike, indicating that the triangular lattice of skyrmions is orientationally disordered. As the temperature is lowered, the ringlike SANS pattern gradually changes to four broad spots along the [−111] and [1−11] directions. The scattering intensity is plotted as a function of azimuthal angle ϕ in Fig. 6(c). Clearly, four peaks around $\phi = 55°$, 125°, 235°, and 305° emerge out of a rather featureless profile at 412 K as the temperature is lowered down to 1.5 K [58].

The four-spot SANS pattern observed at low temperatures is expected for a rhombic lattice of skyrmions with double-$\boldsymbol{q}$ vectors $\parallel \langle 111 \rangle$ that are rotated by 110° from each other as schematically illustrated in Figs. 6(a) and 1(d). The SANS intensity integrated over the region close to the [−111] and [1−11] directions under FC is plotted against temperature together with the intensity integrated around the [001] and [−110] directions in Fig. 6(d). Below 360 K the intensity around the [−111] and [1−11] directions becomes higher than that around the [001] and [−110] directions. This temperature corresponds to the onset of a triangular-rhombic lattice structural transition and is plotted with a purple diamond (right one) in the state diagram in Fig. 2(b). The broad SANS pattern and the gradual temperature evolution indicate the coexistence of the triangular and rhombic SkX states over a wide temperature region.

The transformation to the rhombic lattice is probably driven by the significant enhancement of magnetocrystalline anisotropy at low temperatures that favors $\boldsymbol{q} \parallel \langle 111 \rangle$ as found for the helical state (Fig. 5). It is also noted that the absolute value of q slightly increases upon lowering temperature as plotted in Fig. 3(e). The relation between the lattice transformation and the change in the q value is discussed further in the summary section concerning metastable SkXs (Sec. III F 2).

4. *Metastability of skyrmions against field variation*

We also investigated the metastability and the lattice form of skyrmions against field variation. The detailed field-dependent SANS data at 300 K after the FC (0.03 T) are presented in the Supplemental Material [57], Fig. S2. When field sweeping towards the positive direction, the four broad-spot pattern with stronger intensity at the [−111] and [1−11] directions changes to a uniform ring above 0.1 T as observed for the equilibrium SkX phase at 412 K and 0.03 T. This field variation corresponds to the change in skyrmion lattice form from the rhombic one to the original, albeit disordered triangular one. Importantly, such a ringlike pattern is never observed upon the field sweeping at 300 K after ZFC. This result ensures that the broad four-spot pattern appearing after the FC is attributed to the metastable rhombic SkX (M-R-SkX) and distinct from the helical multidomain state. The SANS intensity originating from the disordered triangular SkX persists up to the region close to the field-induced ferromagnetic phase, which is also in contrast to the helical state. When field sweeping toward negative direction, on the other hand, the scattering intensity around the [−111] and [1−11] directions further increases, and the four-spot pattern becomes clearer. This indicates that the rhombic lattice is more stable than the triangular one at zero or negative fields. As the field is swept further negative, the SANS intensity from the rhombic

SkX finally disappears upon the transition to the equilibrium conical phase.

The field variation at 1.5 K after the FC (0.03 T) is displayed in the Supplemental Material [57], Fig. S3, where similar changes in the SANS patterns are observed, while the four broad spots persist over a wider field region than that seen at 300 K.

The field variations of the SANS data at 300 and 1.5 K are consistent with those of ac susceptibility, where smaller values (as compared with conical phase) corresponding to the metastable SkX are observed, accompanied by a characteristic asymmetric hysteresis. Similar field-dependent ac susceptibility measurements after FC processes were performed at different temperatures, and the determined boundaries of the metastable SkX state are plotted in the T-H phase diagram in Fig. 2(b). The metastable SkX state persists over a wide T-H region, including room temperature and zero field. Within the metastable state, the lattice form of skyrmions undergoes the transition from triangular to rhombic at a low-T and low-H region where $\boldsymbol{q}$ vector anisotropy along $\langle 111 \rangle$ is significant.

C. $Co_8Zn_8Mn_4$

In this section, we describe detailed results of SANS measurements with an off-axis field configuration in $Co_8Zn_8Mn_4$ that provides evidence for increased magnetocrystalline anisotropy that favors $\boldsymbol{q} \parallel \langle 100 \rangle$ at low temperatures.

1. Temperature-driven structural transition of metastable skyrmion lattice

First, we review the temperature variation of the metastable SkX under a field parallel to the [001] direction, as reported in our previous paper [34] (see Supplemental Material, Fig. S5, for the details [57]). In the FC process at 0.04 T, the SANS pattern transforms from 12 spots to 4 spots below 120 K. The 12-spot pattern at high temperatures corresponds to a two-domain triangular SkX state, in which one of the triple $\boldsymbol{q}$-vectors is parallel to the [010] or [100] direction. The four-spot pattern at low temperatures is attributed to a square SkX state with double-$\boldsymbol{q}$ vectors parallel to the [010] and [100] directions. This temperature variation is reversible, and the triangular SkX revives already at 200 K in the subsequent rewarming process, which rules out the possibility of relaxation to a helical multidomain state. It is noted that the transformation to the square SkX below 120 K is accompanied by a large increase in q as presented in Fig. 3(g).

2. Temperature-dependent magnetic anisotropy as revealed by an off-axis field measurement

Next, we show how the $\boldsymbol{q}$-vector orientation changes during the triangular-square structural transition of the skyrmion lattice under an off-axis magnetic field (Fig. 7). The experimental configuration for the SANS measurement is illustrated in Fig. 7(a). The magnetic field of 0.03 T was applied along a direction tilted by 15° away from [001]. While keeping this configuration, the cryomagnet and the sample were rotated together around the vertical [010] direction. Here, ω is defined as a rocking angle between the incident neutron beam (k_i) and the applied magnetic field (H), namely, $\omega = 0°$ for $k_i \parallel H$ and $\omega = -15°$ for $k_i \parallel [001]$.

Rocking curves (SANS intensity versus ω) at selected temperatures are presented in Fig. 7(b). Here, integrated intensity at $\phi = 90°$ and 270° is plotted against ω. For the equilibrium triangular SkX state, a rocking curve is expected to take a maximum close to $\omega = 0°$ because the triple $\boldsymbol{q}$-vectors are usually perpendicular to the applied field regardless of the crystal orientation. However, the observed rocking curve at 295 K [red symbols in Fig. 7(b)] shows a broad maximum around $\omega \sim 20°$. This indicates that, as shown in Fig. 7(a), the effective magnetic field inside the sample ($H_{\rm eff}$) is further tilted from the external field to the opposite side of the [001] axis, which can be understood in terms of a demagnetization effect in the present rectangular-shaped sample [60]. As the temperature is lowered, the peak position of the rocking curve shifts to lower angle and eventually locates at −15° by 40 K.

The temperature variations of the SANS patterns for $k_i \parallel H_{\rm eff}$ and $k_i \parallel [001]$, averaged over the rocking angles of $14° \leqslant \omega \leqslant 20°$ and $-20° \leqslant \omega \leqslant -10°$, respectively, are shown in Figs. 7(c) and 7(d). For $k_i \parallel H_{\rm eff}$, a six-spot pattern is observed at 295 K. This six-spot pattern corresponds to a single-domain triangular SkX state, in which the triple $\boldsymbol{q}$-vectors are all perpendicular to $H_{\rm eff}$ and one of them is parallel to the vertical [010] direction. The six spots are still discerned at 200 K as the triangular SkX persists as a metastable state. At 120 K, the four side spots become much weaker as compared with the two vertical spots, and finally the six-spot pattern is not discerned at 40 K. For $k_i \parallel [001]$, on the other hand, only the two vertical spots out of the six spots are observed at 295 K. Below 120 K, spot intensities around the horizontal region increase, and finally a four-spot pattern is observed at 40 K.

The SANS intensity for the two different configurations is plotted against temperature in Fig. 7(e), clearly showing the change in intensity distribution below 120 K from the four side spots perpendicular to $H_{\rm eff}$ (blue circles) to the two side spots parallel to the [100] direction (red squares), in good accord with the large shift of the peak position in the rocking curves presented in Fig. 7(b). Therefore, the double $\boldsymbol{q}$-vectors of the square SkX at low temperatures are aligned to the [010] and [100] directions, and the latter is not perpendicular to $H_{\rm eff}$. This is in marked contrast to the triangular SkX state at high temperatures where all the triple-$\boldsymbol{q}$ vectors are perpendicular to $H_{\rm eff}$. Thus, the triangular-square SkX transition under the off-axis field is accompanied by a reorientation of skyrmions as schematically illustrated in Fig. 7(f). This result indicates that the magnetic anisotropy favoring $\boldsymbol{q} \parallel \langle 100 \rangle$ is strongly enhanced during the transformation to the square SkX as the temperature is reduced.

D. $Co_9Zn_9Mn_2$

In this section, we present how the $\boldsymbol{q}$ vector evolves in terms of magnitude and orientation as a function of temperature in $Co_9Zn_9Mn_2$. In brief, the change in $\boldsymbol{q}$ direction, and the variation of q value, are qualitatively similar to those found in $Co_8Zn_8Mn_4$ but take place at lower temperatures.

1. Temperature dependence of metastable SkX

First, we show the temperature variation of the metastable SkX state (Fig. 8). Selected SANS patterns in a FC process

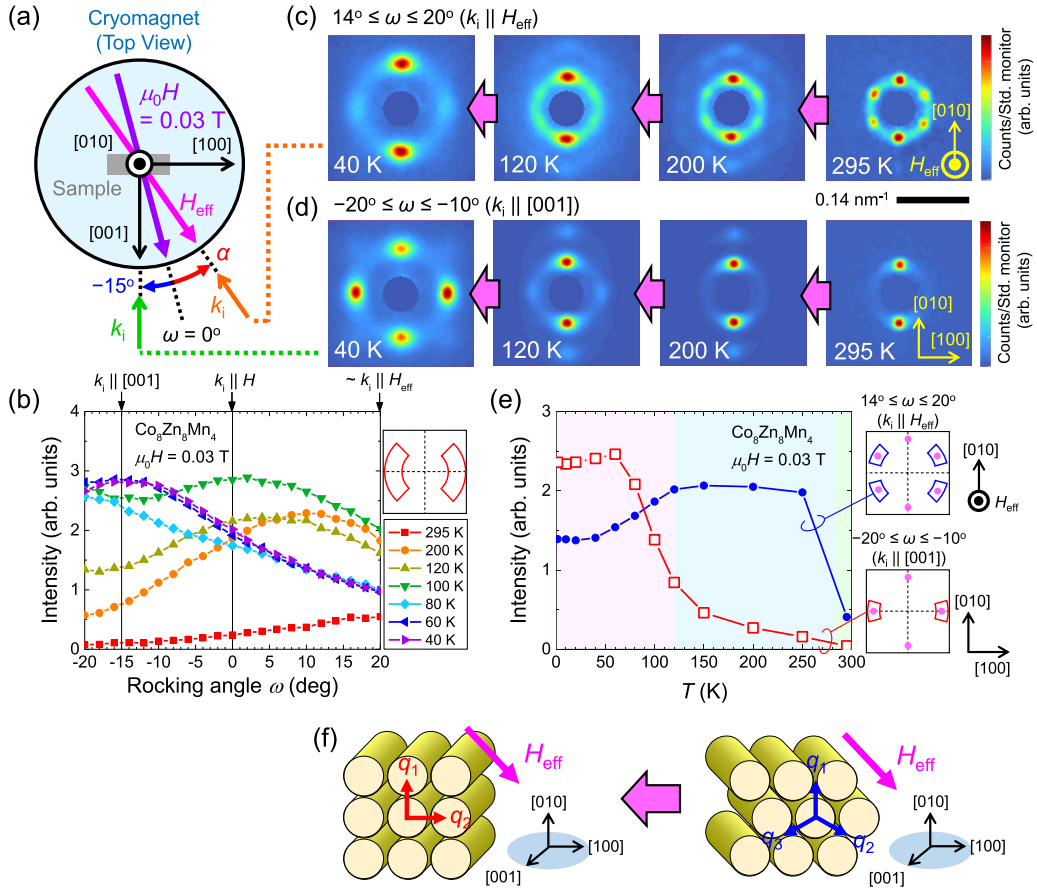

FIG. 7. Reorientation of metastable SkX at low temperatures in $Co_8Zn_8Mn_4$ under an off-axis field. (a) Schematic top view of the experimental configuration. Rocking angle (ω) is defined as the angle between the incident neutron beam (k_i) and the applied magnetic field (H). In this experiment, the magnetic field was tilted by 15° away from the [001] direction. Due to the demagnetization effect from the tilted magnetic field applied to the rectangular-shaped sample (gray object), the effective magnetic field (H_{eff}, pink arrow) inside the sample is tilted by more than 15° from [001] direction. The additional tilting angle (α) of H_{eff} from H is estimated to be $\alpha \sim 20°$ according to both the calculation of the demagnetization field [60] and the peak position of the rocking curve at 295 K shown in (b). (b) Rocking curves at selected temperatures in the field-cooling (FC) process. SANS intensities are integrated over the azimuthal angle area at $\phi = 90°, 270°$ with the width of $\Delta\phi = 90°$ (red areas in the inset). (c), (d) SANS images at 295, 200, 120, and 40 K during a FC process at 0.03 T. These SANS images are summed over the limited rocking angles: (c) $14° \leqslant \omega \leqslant 20°$ (around H_{eff}) and (d) $-20° \leqslant \omega \leqslant -10°$ (around [001]). The intensity scale of the color plot varies between each panel. (e) Temperature dependence of the SANS intensities during the FC process. Blue closed circles show the SANS intensity integrated over the azimuthal angle areas at $\phi = 60°, 120°, 240°, 300°$ with widths of $\Delta\phi = 30°$ in the rocking angle range of $14° \leqslant \omega \leqslant 20°$ (blue areas in the inset). Red open squares represent the SANS intensity integrated over the azimuthal angle areas at $\phi = 90°, 180°$ with widths of $\Delta\phi = 30°$ in the rocking angle range of $-20° \leqslant \omega \leqslant -10°$ (red areas in the inset). The temperature regions of the equilibrium triangular SkX, metastable triangular SkX, and metastable square SkX are indicated with the light green, light blue, and pink shadings, respectively. (f) Schematic illustration of transformation from a triangular SkX to a square SkX under the off-axis effective field H_{eff} tilted from [001]. While the skyrmions in the triangular SkX are parallel to H_{eff}, those in the square SkX at low temperatures are parallel to [001].

at 0.04 T from 390 to 10 K are displayed in Fig. 8(b). In this measurement, the magnetic field and the incident neutron beam are parallel to the [110] direction. At 390 K within the equilibrium SkX phase, the SANS pattern shows six spots, corresponding to a triangular SkX with one of triple $\boldsymbol{q}$-vectors || [001] as illustrated in the right panel of Fig. 8(a). The triangular SkX persists down to 100 K as a metastable state during the FC. Below 50 K, the signal from the four side spots becomes weaker as compared with the vertical two spots, as similarly observed in the off-axis field measurement for $Co_8Zn_8Mn_4$ [Fig. 7(b)].

Figure 8(d) shows the temperature dependence of the SANS intensity for the four side spots and the two vertical spots, clearly showing the cross correlation between the reduced intensity for the four side spots and the increased intensity for the [001] direction below 50 K. Rocking curves during the FC are displayed in Fig. 8(c). While the rocking curve exhibits a peak around $\omega = 0°$ above 100 K, the intensity around $\omega = 0°$ decreases below 50 K and finally the rocking curve forms a concave shape around $\omega = 0°$ at 10 K. These results are similar to those observed from the SANS data for $Co_8Zn_8Mn_4$ under the off-axis field as shown in Fig. 7. Therefore, we attribute the change in the SANS pattern below 50 K in $Co_9Zn_9Mn_2$ to the $\boldsymbol{q}$-vector reorientation and associated transition from a triangular SkX to a square SkX. Namely, one of the double $\boldsymbol{q}$ forming the square SkX is

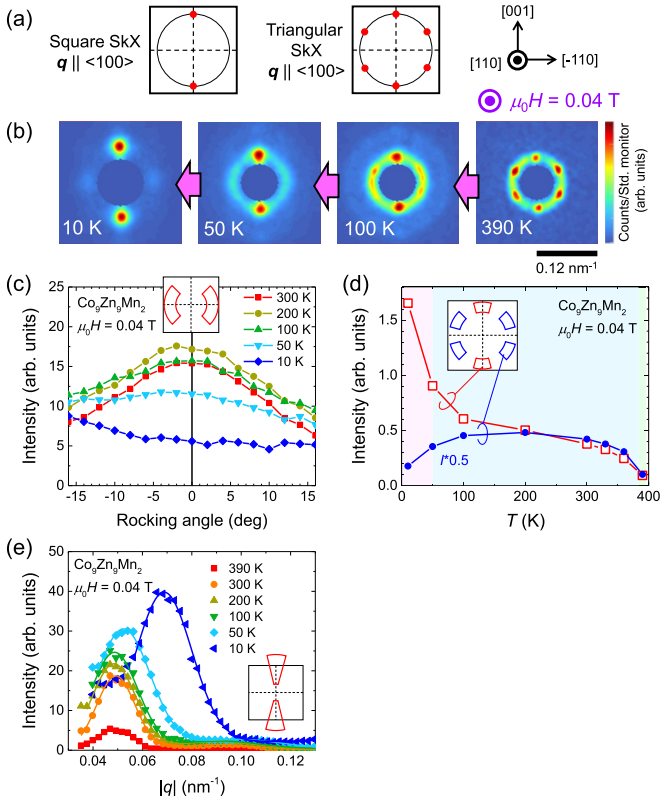

FIG. 8. Metastable SkX state in $Co_9Zn_9Mn_2$. (a) Schematic SANS pattern on the (110) plane, perpendicular to the field, expected for a triangular SkX state (right panel) and for a square SkX state (left panel). The triangular SkX state with one of triple $\boldsymbol{q}$-vectors ∥ [001] shows six spots at $\phi = 0°$, 60°, 120°, 180°, 240°, 300°. Here, ϕ is defined as the clockwise azimuthal angle from the vertical [001] direction. The square SkX state with double $\boldsymbol{q}$-vectors ∥ [001] and ∥ [100] or [010] (out of the plane) exhibits two spots at $\phi = 0°$, 180°. (b) SANS images observed at 390, 100, 50, and 10 K in the field-cooling (FC) process at 0.04 T. The intensity scale of the color plot varies between each panel. The magnetic field was applied at 390 K after zero field cooling. (c) Rocking curves at selected temperatures in the FC process. SANS intensities are integrated over the azimuthal angle areas at $\phi = 90°$, 270° with widths of $\Delta\phi = 90°$ (red areas in the inset). The origin of the rocking angle ($\omega = 0°$) corresponds to $k_i \parallel H \parallel$ [110]. (d) Temperature dependence of the SANS intensities. Blue closed circles show the SANS intensity integrated over the azimuthal angle areas at $\phi = 60°$, 120°, 240°, 300° with widths of $\Delta\phi = 30°$ (blue area in the inset) and finally divided by 2. Red open squares represent the SANS intensity integrated over the azimuthal angle areas at $\phi = 0°$, 180° with widths of $\Delta\phi = 30°$ (red areas in the inset). The temperature regions of the equilibrium triangular SkX, metastable triangular SkX, and metastable square SkX are indicated with the light green, light blue, and pink shadings, respectively. (e) Radial $|q|$ dependence of SANS intensity, integrated over the azimuthal angle areas at $\phi = 0°$, 180° with widths of $\Delta\phi = 30°$ (red areas in the inset), at several temperatures during the FC process. The data points are fitted to a Gaussian function (solid lines).

aligned to the [001] direction but the other is aligned to [100] or [010] directions that are out of the (110) plane, resulting in two vertical spots on the (110) plane as illustrated in the left panel of Fig. 8(a).

The radial q dependence of the SANS intensity for the [001] direction is shown in Fig. 8(e). While the peak center ($q \sim 0.05$ nm^{-1}) is almost temperature independent above 100 K, a large shift up to $q \sim 0.07$ nm^{-1} is observed below 50 K, accompanied by a slight broadening of the width. Thus, the transition from the triangular SkX to the square SkX in $Co_9Zn_9Mn_2$ is accompanied by increases in the magnitude and width of the $\boldsymbol{q}$ vector, again similarly as observed in $Co_8Zn_8Mn_4$.

2. Field dependence of metastable SkX

Next, we discuss the field variation of the $\boldsymbol{q}$ vector in the metastable SkX state at 10 K after the FC under 0.04 T (see Supplemental Material, Fig. S6, for the details [57]). With increasing field from 0.04 to 0.3 T, the two-spot SANS pattern gradually changes to a ringlike one, in which the scattering intensity lies in the (110) plane as similarly observed at high temperatures. This indicates that the square SkX with $\boldsymbol{q} \parallel \langle 100 \rangle$ at low temperatures transforms to an orientationally disordered triangular SkX with $\boldsymbol{q} \perp H$ at high fields.

Taking the above results into account, we summarize the state diagram of the metastable SkX in $Co_9Zn_9Mn_2$ in Fig. 2(c), which is characterized by a large region of the triangular SkX state and a small region of the square SkX state existing only at low temperatures below ∼50 K and low fields.

E. $Co_7Zn_7Mn_6$

In this section, we discuss how the magnetic state is affected by the increased Mn concentration in $Co_7Zn_7Mn_6$.

1. Heavily disordered square lattice within the metastable state

First, we discuss the temperature variation of the metastable SkX (Fig. 9). Figure 9(b) shows the change in the SANS patterns during a FC at 0.025 T from 146 to 1.5 K. In this measurement, the magnetic field and the incident neutron beam are parallel to the [001] direction. At 146 K within the equilibrium SkX phase, a 12-spot pattern corresponding to a two-domain triangular SkX with one of triple $\boldsymbol{q}$-vectors ∥ [010] or [100], as schematically illustrated at right panel in Fig. 9(a), is observed. However, the spots display a significant azimuthal broadening as compared with those observed from the equilibrium SkX in the $Co_8Zn_8Mn_4$ sample. The 12-spot pattern changes to a pattern of four broadened spots at 100 K, which corresponds to a metastable square SkX with double $\boldsymbol{q}$-vectors ∥ [010] and [100] as shown in the left panel in Fig. 9(a). With further decreasing temperature down to 60 K, the four spots become even broader. This pattern of four very broad spots remains almost unchanged across the reentrant spin-glass transition ($T_g \sim 30$ K) down to 1.5 K.

The SANS intensity from the metastable SkX is plotted as a function of temperature in Fig. 9(c). Above 130 K, the intensities integrated for directions close to ⟨100⟩ and ⟨110⟩ show similar values as expected for a 12-spot pattern. Below 120 K, the intensity for ⟨100⟩ becomes larger than that for ⟨110⟩ due to the change in the pattern from 12 spots to 4 spots. The intensities for both regions significantly decrease below 120 K, and become similar again below 60 K, which corresponds to the pronounced broadening of the 4 spots.

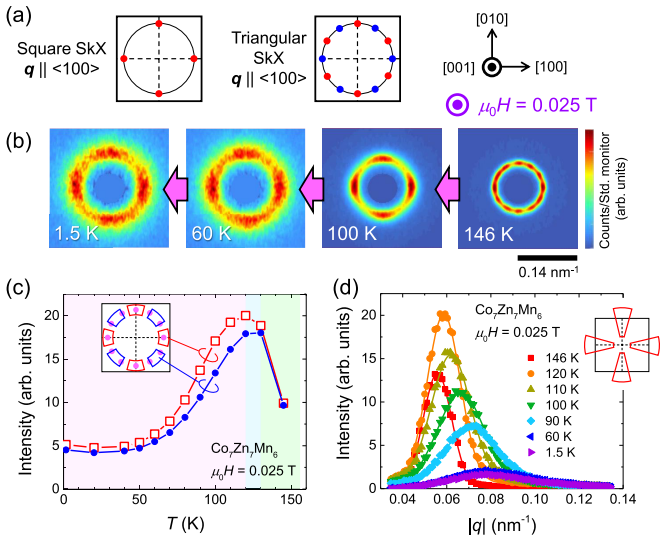

FIG. 9. Temperature dependence of metastable SkX state in $Co_7Zn_7Mn_6$. (a) Schematic SANS pattern on the (001) plane, perpendicular to the field, expected for a triangular SkX state (right panel) and for a square SkX state (left panel). The triangular SkX state forms two domains with one of the triple $\boldsymbol{q}$-vectors ∥ [100] (6 blue spots) and ∥ [010] (6 red spots), respectively, resulting in 12 spots separated every 30° from $\phi = 0°$. Here, ϕ is defined as the clockwise azimuthal angle from the vertical [010] direction. The square SkX state with double $\boldsymbol{q}$-vectors ∥ [100] and [010] shows 4 spots at $\phi = 0°, 90°, 180°, 270°$. (b) SANS images observed at 146, 100, 60, and 1.5 K during the field-cooling (FC) process at 0.025 T. The intensity scale of the color plot varies between each panel. The magnetic field was applied at 146 K after zero field cooling. (c) Temperature dependence of the SANS intensities. Blue closed circles show the SANS intensity integrated over the azimuthal angle areas at $\phi = 45°, 135°, 225°, 315°$ with widths of $\Delta\phi = 30°$ (blue areas in the inset). Red open squares represent the SANS intensity integrated over the azimuthal angle areas at $\phi = 0°, 90°, 180°, 270°$ with widths of $\Delta\phi = 30°$ (red areas in the inset). The temperature regions of the equilibrium triangular SkX, metastable triangular SkX, and metastable square SkX are indicated with the light green, light blue, and pink shadings, respectively. (d) Radial $|q|$ dependence of SANS intensity, integrated over the azimuthal angle areas at $\phi = 0°$, 90°, 180°, 270° with widths of $\Delta\phi = 30°$ (red areas in the inset), at several temperatures in the FC process. The data points are fitted to a Gaussian function (solid line).

Therefore, while the triangular-square SkX transition occurs below 120 K in common with $Co_8Zn_8Mn_4$, the square SkX is more severely disordered below ∼90 K. This is in accord with the disordering of the helical state of Co spins below ∼90 K on ZFC [31] due to the development of short-range antiferromagnetic correlations of Mn spins.

The radial q dependence of the SANS intensity for ⟨100⟩ is presented in Fig. 9(d). From 120 to 60 K, where the triangular-square SkX transition occurs, the peak center exhibits a large shift from 0.06 to 0.08 nm^{-1}, and the magnitude and width of the peak significantly decrease and increase, respectively. Thus, the triangular-square structural transformation of SkX in $Co_7Zn_7Mn_6$ is also accompanied by the large increase in q as well as in its width. This indicates that the metastable SkX is heavily disordered, similarly to the helical state during ZFC [Fig. 3(l)].

2. *Field dependence of metastable SkX*

Next, we discuss how the metastable SkX state varies with field sweeping in the well-ordered region at 100 K (Fig. 10) and in the disordered region at 60 K (Fig. 11). Figure 10(a) shows the field variation in the SANS patterns at 100 K after a field cooling (FC) at 0.025 T. The detailed field dependence of the SANS intensity integrated over the regions around ⟨100⟩ and ⟨110⟩ is displayed in Fig. 10(c). Upon increasing the field to the positive direction, the initial four-spot pattern changes to a uniform ring above 0.055 T, where the scattering intensities for ⟨100⟩ and ⟨110⟩ completely overlap while showing a clear shoulder, and the signal persists up to 0.1 T. This change is ascribed to the transformation from the square SkX to an orientationally disordered triangular SkX similar to the case of $Co_8Zn_8Mn_4$ [34]. On field sweeping to the negative direction, the four-spot pattern again changes to the ringlike one at −0.055 T but the intensity is much weaker than that observed at 0.055 T. In the returning process from 0.15 to 0 T, a clear SANS signal is not observed because the metastable SkX is completely destroyed in the high-field region and a conical phase is stabilized instead. The large and asymmetric hysteresis of the intensity plot in Fig. 10(c) is thus attributed to the existence of the metastable SkX state. For comparison, the field dependence of the SANS pattern and the integrated intensity at 100 K after zero-field cooling is shown in Figs. 10(b) and 10(d), respectively. In this case, four spots corresponding to the helical multidomain state with $\boldsymbol{q}$-vectors ∥ ⟨100⟩ are observed up to 0.05 T, but the signal disappears at 0.1 T without exhibiting a clear ringlike patten. This field variation of the helical state after ZFC is totally different from that observed after the FC. Therefore, it can be concluded that the metastable SkX created by the FC survives over a wide field region at 100 K, and the square SkX changes to the triangular SkX at high fields.

We also show the field variation of the metastable SkX state at 60 K in Fig. 11, and discuss another transition to the second equilibrium skyrmion phase. The field-dependent SANS patterns at 60 K after FC (0.025 T) are presented in Fig. 11(a). The SANS intensity integrated over the region around ⟨100⟩ and ⟨110⟩ in this process is plotted against magnetic field in Fig. 11(c). As the field is increased to the positive direction, the initial pattern with four broad spots originating from the disordered square SkX changes to a broad ring pattern above 0.07 T, resulting in almost equal scattering intensities for ⟨100⟩ and ⟨110⟩. On field sweeping to the negative-field region, the broad ring pattern with similar intensity is observed at −0.07 and −0.1 T. Therefore, the field variation after FC is less asymmetric between the positive and negative fields as compared with the result at 100 K. In the returning process from the field-induced ferromagnetic phase (±0.2 T) down to 0 T, the broad ring pattern appears again and remains down to zero field. Note that the intensity of the ring pattern around zero field is relatively large and comparable to that of the initial broad four-spot pattern just after the FC. For comparison, we show SANS patterns observed at the same magnetic fields after ZFC in Fig. 11(b), and the field dependence of the

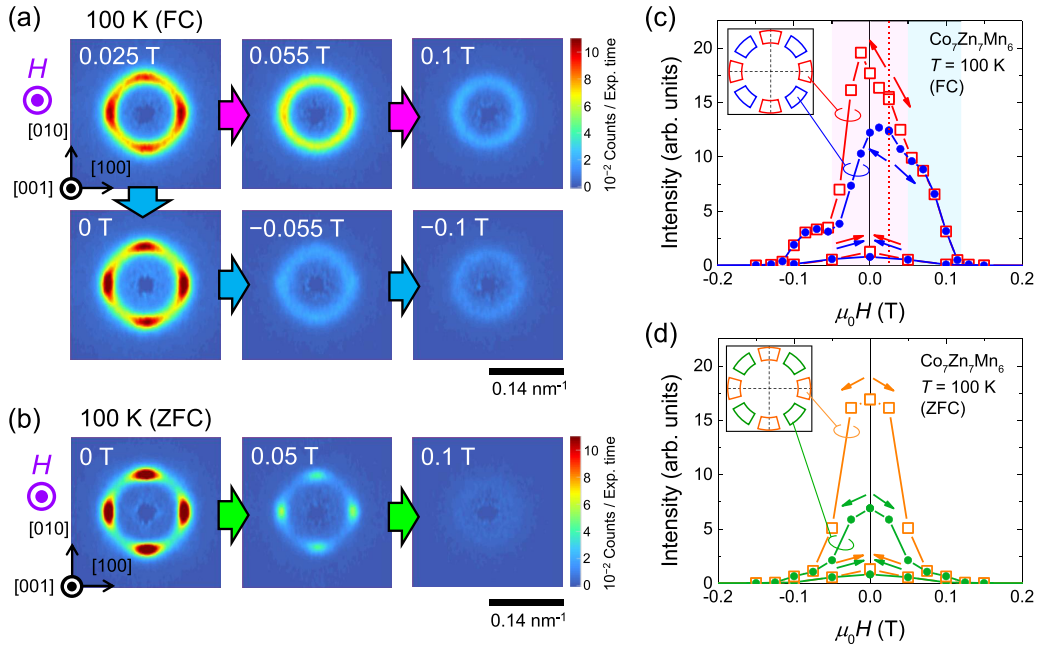

FIG. 10. Field effect on metastable SkX state and helical state in $Co_7Zn_7Mn_6$ at 100 K. (a) SANS images at selected fields during field scans to positive and negative directions at 100 K after a field cooling (FC) at 0.025 T. (b) SANS images observed at 0, 0.05, and 0.1 T at 100 K after a zero-field cooling (ZFC) (reproduced from our previous work in Ref. [31], Copyright 2018, American Association for the Advancement of Science). The intensity scale of the color plot is fixed for all the panels in (a) and (b). (c) Field dependence of the SANS intensities at 100 K after the FC defined similarly as in Fig. 9(c). The field regions of the metastable triangular SkX and the metastable square SkX are indicated with the light blue and pink shadings, respectively. (d) Field dependence of the SANS intensities at 100 K after the ZFC (reproduced from our previous work in Ref. [31], Copyright 2018, American Association for the Advancement of Science). Green closed circles show the SANS intensity integrated over the azimuthal angle areas at $\phi = 45°, 135°, 225°, 315°$ with widths of $\Delta\phi = 30°$ (green areas in the inset). Orange open squares represent the SANS intensity integrated over the azimuthal angle areas at $\phi = 0°, 90°, 180°, 270°$ with widths of $\Delta\phi = 30°$ (orange areas in the inset).

SANS intensity is plotted in Fig. 11(d). In this process, the broad four-spot pattern (disordered helical state) changes to a broad ring above 0.07 T similar to the FC case. The field dependence commonly observed for the FC (both for positive and negative-field directions) and ZFC processes is in accord with the existence of another field-induced equilibrium phase at low temperatures. In our previous study on $Co_7Zn_7Mn_6$, the broad ring pattern at low temperatures has been identified to be a three-dimensionally disordered skyrmion phase, which are stabilized by the frustrated magnetism of Mn spins and exist as an equilibrium phase that is distinct from the conventional SkX phase just below T_c [31]. Therefore, the observed change from the broad four-spot pattern to the broad ring pattern above 0.07 T in the FC case corresponds to the transition from the metastable square SkX state (originating from the high-temperature equilibrium SkX phase) to the other equilibrium disordered skyrmion phase. The ring pattern remaining at zero field after the field decreasing process is explained in terms of metastable skyrmions that are created initially in the high-field region and persist down to zero field.

On the basis of the above results, the state diagram of the metastable SkX in $Co_7Zn_7Mn_6$ is summarized in Fig. 2(e). The metastable square SkX (M-S-SkX) state exists below 120 K and at low fields inside the metastable triangular SkX (M-T-SkX) state. In addition, the equilibrium disordered skyrmion (E-DSk) phase is stabilized at low temperatures just above the reentrant spin-glass transition around 30 K. Note that the E-DSk phase is discerned also in a negative-field region, reflecting its thermodynamic equilibrium nature.

F. Summary of helical state and metastable skyrmion state

Taking the SANS results for all the compounds into account, we come back to Figs. 2 and 3 again and discuss how the helical and metastable skyrmion states change with Mn concentration.

1. Correspondence between magnetization and q vector in helical state

Table I summarizes the several quantities that characterize the helical state. One important effect of Mn substitution is the change in $\boldsymbol{q}$-vector direction: while the preferred orientations of $\boldsymbol{q}$-vectors are ⟨111⟩ directions in $Co_{10}Zn_{10}$, they are ⟨100⟩ directions in all the Mn-doped compounds. The helical structure is formed by ferromagnetically coupled Co spins accompanied with DMI, but as described in Table I (see also Supplemental Material [57], Fig. S1), the saturation magnetization M_s measured at 2 K and 7 T takes a maximum at $Co_9Zn_9Mn_2$. This suggests that Co and Mn are ferromagnetically coupled at least in the low Mn concentration region, as also demonstrated recently by x-ray magnetic circular dichroism (XMCD) measurements [61].

Mn substitution produces another important effect: Figs. 3(e)–3(h) summarize the temperature dependence of the

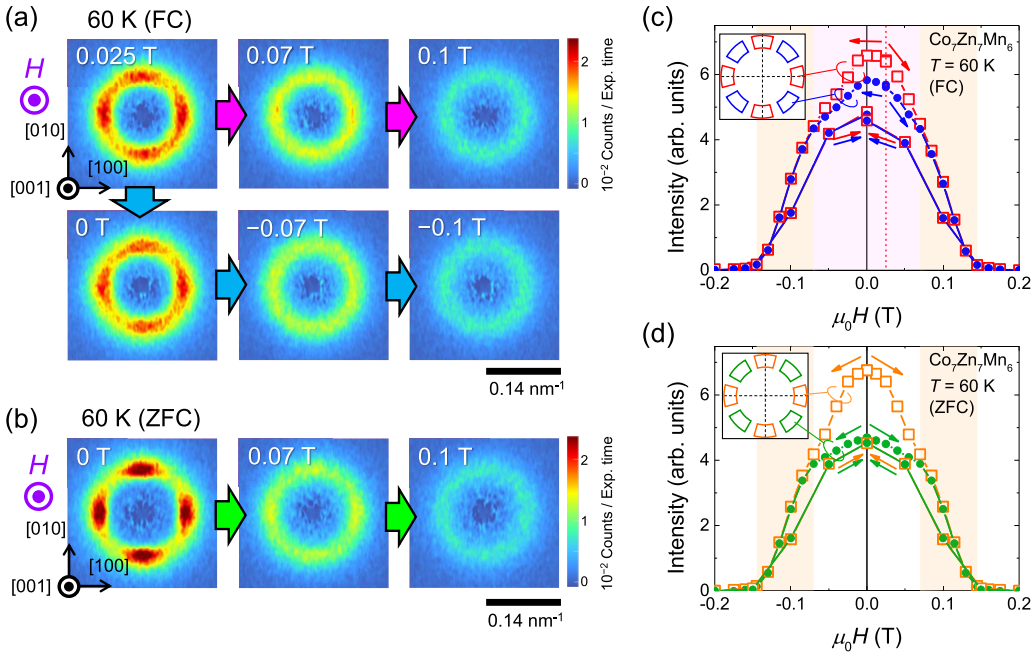

FIG. 11. Metastable and low-temperature equilibrium skyrmion states in magnetic fields in $Co_7Zn_7Mn_6$ at 60 K. (a) SANS images at selected fields during field scans to positive and negative directions at 60 K after a FC at 0.025 T. (b) SANS images observed at 0, 0.07, and 0.1 T at 60 K after a ZFC. The intensity scale of the color plot is fixed for all the panels in (a) and (b). (c) Field dependence of the SANS intensities at 60 K after FC, integrated over the azimuthal angle areas defined similarly as in Fig. 9(c). The field regions of the metastable square SkX and the equilibrium disordered skyrmion (DSk) phase are indicated with the pink and orange shadings, respectively. (d) Field dependence of the SANS intensities at 60 K after the ZFC (reproduced from our previous work in Ref. [31], Copyright 2018, American Association for the Advancement of Science), integrated over the azimuthal angle areas defined similarly as in Fig. 10(d). The field region of the equilibrium DSk phase is indicated with orange shading.

helical q value measured for all the compounds. The q value was determined as the peak center of a Gaussian function fitted to the azimuthal-angle-averaged SANS intensity as a function of q. In $Co_{10}Zn_{10}$, q gradually and slightly increases by only ∼10% upon cooling from T_c to low temperatures. On the other hand, $Co_9Zn_9Mn_2$ shows a large increase in q below 50 K by ∼45% while for $Co_8Zn_8Mn_4$ and $Co_7Zn_7Mn_6$, q also displays a large increase of ∼50% below 120 K. Notably, the large observed increases in q almost coincide with the gradual decrease in M from T_H to T_L as shown in Figs. 3(a)–3(d). The temperature region where q significantly varies is indicated in the T-x phase diagram in Fig. 1(b).

Figures 3(i)–3(l) show the temperature dependence of the full width at half-maximum (FWHM) of the Gaussian function fitted to the SANS intensity versus q, which provides a measure of the spatial coherence of the helimagnetic order. The FWHM increases upon cooling in all the compositions while showing strong correlation with the increase in the magnitude of q value [Figs. 3(e)–3(h)]. Among them, $Co_7Zn_7Mn_6$ exhibits a significant increase below ∼90 K, which indicates that the helical state in $Co_7Zn_7Mn_6$ becomes severely disordered at low temperatures. The increase in the FWHM for $Co_9Zn_9Mn_2$ and $Co_8Zn_8Mn_4$ also indicates the evolution of magnetic disorder to some extent, although it appears to be less significant as compared with $Co_7Zn_7Mn_6$.

The above temperature and Mn concentration dependence of helical states is well explained by the interplay between the ferromagnetically coupled Co spins forming the helical state and antiferromagnetically coupled Mn spins. Namely, the significant increase in the q value (or decrease in the helical periodicity) at low temperatures is caused by the effective decrease in the ratio of the ferromagnetic exchange interaction to the DMI, which is attributed to short-range antiferromagnetic correlations of Mn spins. These short-range correlations act as a source of disorder for helimagnetic Co spins, and start to develop at increasingly higher temperature (higher T/T_c) as the Mn concentration is increased. The increase of the q value finally saturates below T_L probably due to a slowing of the antiferromagnetic fluctuations of Mn spins that results in a quasistatic disorder for helimagnetic Co spins. As the temperature is further reduced, Mn spins eventually freeze and undergo the reentrant spin-glass transition as observed in the magnetization measurements for $Co_8Zn_8Mn_4$ and $Co_7Zn_7Mn_6$ [Figs. 3(c) and 3(d)]. The freezing temperature T_g also increases with the Mn concentration due to the associated enhancement of the antiferromagnetic Mn spin correlations.

2. Summary of metastable skyrmion state

Figure 2 summarizes the equilibrium and metastable skyrmion phase diagrams on the T-H plane determined by SANS and ac susceptibility measurements in $Co_{10}Zn_{10}$, $Co_9Zn_9Mn_2$, $Co_8Zn_8Mn_4$, and $Co_7Zn_7Mn_6$. In all compounds, the metastable SkX state is realized by a conventional field cooling via the equilibrium SkX phase just below T_c, and prevails over a very wide temperature and field region. In addition, while the equilibrium and metastable skyrmions

at high temperatures form a conventional triangular lattice described with triple-$\boldsymbol{q}$ vectors, the lattice structure transforms to novel double-$\boldsymbol{q}$ states at low temperatures as follows. In $Co_{10}Zn_{10}$ [Fig. 2(b)], the lattice form of the metastable SkX transforms from a triangular to a rhombic one (M-R-SkX) with double $\boldsymbol{q}$-vectors $\parallel \langle 111 \rangle$ below ∼360 K with a broad coexistence region (the purple region). At all temperatures, the triangular lattice is restored as the field is increased. In $Co_9Zn_9Mn_2$ [Fig. 2(c)], while the triangular lattice of the metastable skyrmions (M-T-SkX) persists over a wide temperature region, it transforms to square one (M-S-SkX) with double $\boldsymbol{q}$-vectors $\parallel \langle 100 \rangle$ below ∼50 K as shown with a pink region. The triangular lattice is also recovered at high fields. In $Co_8Zn_8Mn_4$ [Fig. 2(d)] and $Co_7Zn_7Mn_6$ [Fig. 2(e)], the triangular-square transition of the skyrmion lattice occurs below ∼120 K, and the square SkX persists below the reentrant spin-glass transition temperatures as plotted with yellow circles. In $Co_7Zn_7Mn_6$, the metastable square SkX state originating from the conventional SkX phase undergoes another transition to the other frustration-induced equilibrium skyrmion phase (E-DSk; orange region) as the field is increased at temperatures below ∼60 K.

The structural transitions of the skyrmion lattice to the rhombic or square coordinations are perhaps attributed to the enhanced magnetocrystalline anisotropy favoring $\boldsymbol{q} \parallel \langle 111 \rangle$ and $\boldsymbol{q} \parallel \langle 100 \rangle$, respectively. However, a $\boldsymbol{q}$-vector anisotropy alone is not sufficient to drive the lattice structural transition. Importantly, these transformations are accompanied by an increase in absolute value of q: the triangular-rhombic transition in $Co_{10}Zn_{10}$ is observed while the q value slightly increases over a broad temperature range [Fig. 3(e)], and the triangular-square transition in the Mn-doped compounds occurs only when the q values significantly increase below a specific temperature of T_H [Figs. 3(f)–3(h)]. As discussed quantitatively in the following, the increase in q value is crucial for the transformation of the skyrmion lattice in terms of skyrmion density.

The ratio of skyrmion density (number of skyrmions per area) in the rhombic lattice (n_R) to that in the triangular one (n_T) is given by $n_R/n_T = \frac{3\sqrt{3}}{4\sqrt{2}}(a_T/a_R)^2 = \frac{3\sqrt{3}}{4\sqrt{2}}(q_R/q_T)^2$. Here, a_T (q_T) and a_R (q_R) are the lattice constant (the q value) of the triangular and rhombic lattices, respectively. Since the total number of metastable skyrmions that are topologically protected is conserved during the transition from the triangular lattice to the rhombic one ($n_R = n_T$), the lattice constant should decrease (the q value should increase) by the factor of $\sqrt{\frac{4\sqrt{2}}{3\sqrt{3}}} \sim 1.043$ as the temperature is lowered. The q_R value that is consistent with this condition is presented with a dashed purple line in the $q(T)$ plot for $Co_{10}Zn_{10}$ [inset of Fig. 3(e)]. Here, q_T is taken as the q value at 412 K. It is found that the observed small increase in q value during the FC in $Co_{10}Zn_{10}$ easily satisfies the above condition around ∼200 K. This result is in accord with the fact that the transformation to rhombic lattice starts at high temperatures.

In the case of the transition to square lattice in the Mn-doped compounds, on the other hand, the aforementioned condition is more difficult to fulfill. The ratio of the skyrmion density in the square lattice (n_S) to that in the triangular one is given by $n_S/n_T = \frac{\sqrt{3}}{2}(a_T/a_S)^2 = \frac{\sqrt{3}}{2}(q_S/q_T)^2$, where a_S (q_S) is the lattice constant (the q value) of the square lattice. To keep the skyrmion density constant ($n_S = n_T$), the lattice constant should decrease (the q value should increase) by the larger factor of $\sqrt{\frac{2}{\sqrt{3}}} \sim 1.075$. The value of q_S satisfying this condition is denoted with a dashed pink line in the $q(T)$ plots for $Co_9Zn_9Mn_2$, $Co_8Zn_8Mn_4$, and $Co_7Zn_7Mn_6$ [Figs. 3(f)–3(h)]. Here, q_T is taken as the q value in the equilibrium SkX phase. In $Co_9Zn_9Mn_2$ and $Co_8Zn_8Mn_4$, the q value is almost T independent at high temperatures. However, the q value increases significantly, exceeding the necessary q_S value below T_H (∼50 K for $Co_9Zn_9Mn_2$ and ∼120 K for $Co_8Zn_8Mn_4$ and $Co_7Zn_7Mn_6$), which would describe the transformation to the square lattice. This result well explains the observed onset temperature of the transformation to the square lattice. Nevertheless, the observed increase in q around T_L is as large as $q_S/q_T \sim 1.5$, and the skyrmion density becomes too large if we assume a uniform, perfectly ordered square SkX as shown in Fig. 1(e).

Alternatively, the large increase in q under the condition of conserved skyrmion density can be reconciled with either of the following two scenarios: (i) a microscopic phase separation into a square SkX state and a helical phase as schematically illustrated in Fig. 1(f), or (ii) the onset of skyrmion deformation along the ⟨100⟩ directions [Fig. 1(g)]. It should be noted that, for both (i) and (ii), the total number of skyrmions is identical to the original triangular SkX. Although the latter deformed skyrmions have been observed in a thin-plate sample by LTEM [37] and reproduced by a micromagnetic simulation [61], it is difficult to experimentally distinguish between the two scenarios from SANS studies on a three-dimensional bulk sample. In any case, the large increase in q value at low temperatures and the enhanced $\boldsymbol{q}$-vector anisotropy toward $\boldsymbol{q} \parallel \langle 100 \rangle$ cooperatively drive the skyrmion lattice transformation as the metastable triangular SkX phase is cooled down to low temperatures.

It is also noted that the square lattice of (elongated) skyrmions in the present case is distinct from a meron-antimeron square lattice with vanishing topological charge (genuine superposition of orthogonal double-$\boldsymbol{q}$ vectors) as recently observed in a thin-plate sample of $Co_8Zn_9Mn_3$ by LTEM [39]. The meron-antimeron state appears as an equilibrium state just before entering the equilibrium triangular SkX phase near T_c. While the meron-antimeron square lattice is stabilized by the in-plane shape anisotropy characteristic of a thin-plate specimen as theoretically predicted [62,63], the transition to the square SkX in the present case probably originates from magnetocrystalline anisotropy (local magnetization $\parallel \langle 100 \rangle$, which in turn results in $\boldsymbol{q}$-vector anisotropy along ⟨100⟩) as well as the large increase in q, as discussed above.

G. Lifetime of metastable skyrmion

In the former sections, we revealed that the SkX state can persist at low temperatures by a field-cooling process. Since the low-temperature states are only metastable, the SkX should relax to the more stable conical phase with

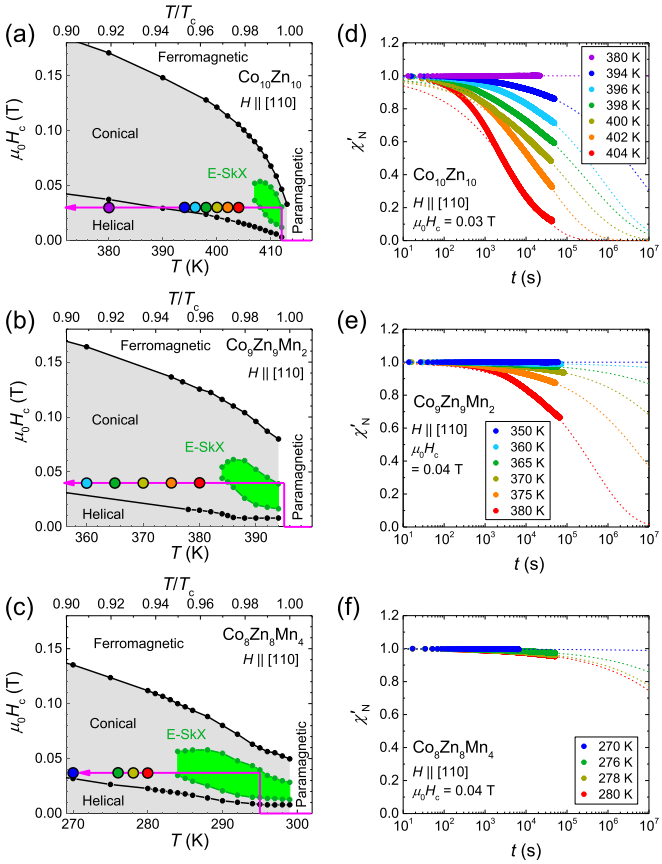

FIG. 12. (a)–(c) Temperature–magnetic field (T-H) phase diagrams near T_c in (a) $Co_{10}Zn_{10}$, (b) $Co_9Zn_9Mn_2$, and (c) $Co_8Zn_8Mn_4$, determined by ac susceptibility (χ') measurements with $H \parallel [110]$. For the magnetic field, calibrated values H_c are used. The displayed range of T/T_c (upper horizontal axis) is fixed to be 0.90–1.01 for the three panels. Time-dependent χ' measurements after a field cooling (FC, pink arrow) via the equilibrium SkX phase (green region) are performed at several temperatures denoted with circles, whose color corresponds to the color of data points in (d)–(f). (d)–(f) Time dependence of the normalized ac susceptibility, defined as $\chi'_N(t) \equiv [\chi'(\infty) - \chi'(t)]/[\chi'(\infty) - \chi'(0)]$, for (d) $Co_{10}Zn_{10}$, (e) $Co_9Zn_9Mn_2$ (reproduced from our previous work in Ref. [36] with permissions, Copyright 2017, American Physical Society) and (f) $Co_8Zn_8Mn_4$, measured in the processes described in (a)–(c). Here, $\chi'(0)$ is an initial value (metastable SkX state), and $\chi'(\infty)$ is the value for the equilibrium conical phase which, as the fully relaxed state is assumed to be the value of χ' at the same magnitude of field after a field decreasing run from a ferromagnetic phase. The data points are fitted to stretched exponential functions (dotted lines) $\exp\{-(t/\tau)^\beta\}$.

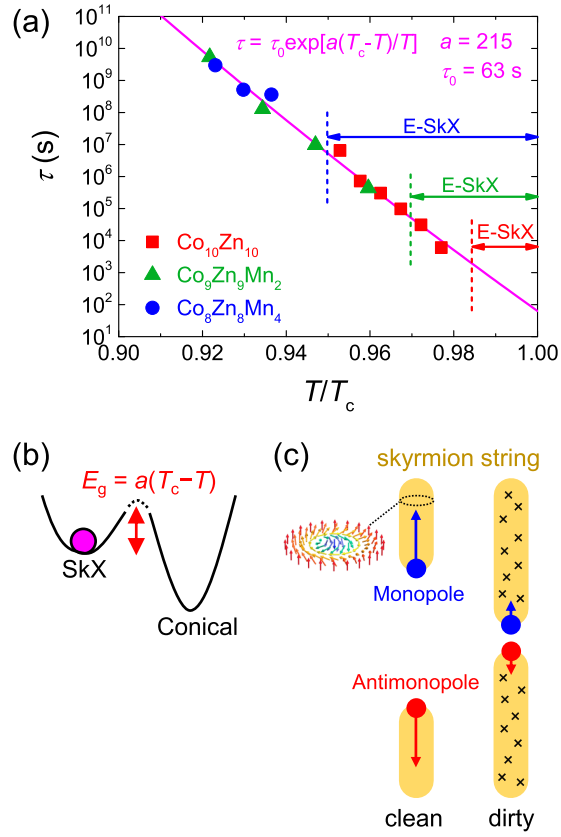

FIG. 13. (a) Relaxation time (τ) of metastable SkX states plotted against normalized temperature T/T_c in $Co_{10}Zn_{10}$ (red squares), $Co_9Zn_9Mn_2$ (green triangles, reproduced from our previous work in Ref. [36] with permissions, Copyright 2017, American Physical Society), and $Co_8Zn_8Mn_4$ (blue circles). The τ values are determined by the fits shown in Figs. 12(d)–12(f). The solid arrows and dotted lines indicate temperature ranges and lower boundaries of equilibrium SkX phases, respectively. The data points from the three different compositions, showing a good scaling, are fitted to a modified Arrhenius law (pink solid line) $\tau = \tau_0 \exp\{a(T_c - T)/T\}$, with an assumption of a temperature-dependent activation energy $E_g = a(T_c - T)$ as described in Refs. [36,64,65]. The parameters obtained from the fitting are $a = 215$ and $\tau_0 = 63$ s. (b) Schematic illustration of free-energy landscape with a metastable SkX state and the more stable conical phase. (c) Schematic illustration of the destruction process for a skyrmion string induced by movement of an emergent monopole-antimonopole pair for a clean system and a dirty system. In the dirty system, the propagations of the monopole and antimonopole are hindered by magnetic disorder while less so in the clean system.

some lifetime. In our previous study (Ref. [36]), we investigated temperature-dependent relaxation times of metastable skyrmions in $Co_9Zn_9Mn_2$ and observed extremely long lifetimes even at high temperatures. For a systematic understanding of behavior, in this section we extend these measurements to the other compounds $Co_{10}Zn_{10}$ and $Co_8Zn_8Mn_4$, and discuss how the metastable SkX lifetime varies with temperature and Mn concentration (Figs. 12 and 13).

Figures 12(a)–12(c) show H-T phase diagrams of equilibrium phases near T_c in $Co_{10}Zn_{10}$, $Co_9Zn_9Mn_2$, and $Co_8Zn_8Mn_4$, respectively. For the purpose of better comparison between the three compounds, T ranges are selected for the respective panels in such a way that a normalized temperature range in T/T_c from 0.90 to 1.01 is shown, as indicated on the upper abscissa. Clearly, the relative size of the equilibrium SkX phase (green region) expands upon increasing the Mn concentration due to the increased chemical and magnetic disorder. After a FC via the equilibrium SkX phase, the temporal variation of ac susceptibility $\chi'(t)$ was measured at a fixed temperature, and this experiment was

TABLE II. Summary of relaxation parameters for metastable SkX in various materials.

Material	a	τ_0 (s)	Reference
Co-Zn-Mn	215	63	This work
MnSi	65	2.7×10^{-4}	[64]
Cu_2OSeO_3	96	3	[65]
Cu_2OSeO_3 (Zn 2.5% doped)	94	150	[65]

repeated at several different temperatures, as denoted with the colored circles.

The normalized ac susceptibility $\chi'_N(t) \equiv [\chi'(\infty) - \chi'(t)]/[\chi'(\infty) - \chi'(0)]$ is plotted as a function of time in Figs. 12(d)–12(f). Here, $\chi'(0)$ and $\chi'(\infty)$ correspond to initial values for the metastable SkX state and the equilibrium conical phase as a fully relaxed state, respectively, such that $\chi'_N = 1$ for $t = 0$ and $\chi'_N = 0$ for $t \rightarrow \infty$. In $Co_{10}Zn_{10}$ [Fig. 12(d)], a clear relaxation from the metastable SkX state to the equilibrium conical phase is observed at 404 K, just below the equilibrium SkX phase, and for which the relaxation time is the order of 10^4 s (several hours). The relaxation time further increases upon lowering the temperature. In $Co_9Zn_9Mn_2$ [Fig. 12(e)], the observed relaxation in the $\chi'_N(t)$ curve within the measurement time (∼1 day) is less than 40% even at 380 K, just below the equilibrium SkX phase, and the relaxation becomes even slower as the temperature is lowered. In $Co_8Zn_8Mn_4$ [Fig. 12(f)], only a few percent relaxation is observed in $\chi'_N(t)$ even at 280 K, just below the equilibrium SkX phase. Therefore, the lifetime of the metastable SkX at temperatures close to the equilibrium SkX phase boundary, for example, the temperatures indicated with the red circles in Figs. 12(a)–12(c), becomes relatively longer as the Mn concentration is increased.

To discuss more quantitatively, the $\chi'_N(t)$ curves are fitted to a stretched exponential function $\exp\{-(t/\tau)^\beta\}$. The obtained β values are in the range of 0.3–0.5, indicating a highly inhomogeneous distribution of relaxation times. The relaxation time τ for all the compounds ($Co_{10}Zn_{10}$, $Co_9Zn_9Mn_2$, and $Co_8Zn_8Mn_4$) is plotted against T/T_c in Fig. 13(a). The τ value increases exponentially as the temperature is lowered, and becomes virtually infinite when T/T_c is less than ∼0.9. Remarkably, the data points from the three different compounds collapse onto a single curve although the applied magnetic field, as well as the respective temperature regions are different. Following the arguments described in Ref. [64], all the data points are fitted to a modified Arrhenius law (pink solid line) $\tau = \tau_0 \exp\{a(T_c - T)/T\}$. Here, the activation energy for the relaxation from the metastable SkX state to the equilibrium conical phase, as schematically illustrated in Fig. 13(b), is assumed to be T dependent as $E_g = a(T_c - T)$ near T_c, instead of constant E_g for standard Arrhenius law. The obtained fitting parameters are $a = 215$ and $\tau_0 = 63$ s. For comparison, the reported values of a and τ_0 for several materials [64,65] are summarized in Table II. Recently, Wild *et al.* reported that τ_0 depends sensitively on the applied magnetic field in their LTEM studies of a thin plate of $Fe_{1-x}Co_xSi$ [66]. For the present ac susceptibility measurements on bulk crystals of Co-Zn-Mn alloys, we used the applied magnetic field for each compound where the SANS intensity from the equilibrium SkX is strongest in the field sweeping measurement. The fact that the τ values from three different compounds collapse onto a single curve (namely, τ_0 are the same) may originate from the fact that the applied field values are close to the optimal ones in the respective samples.

From the obtained value of a, the activation energy E_g is estimated to be larger than 8000 K at a temperature $T = 0.9T_c$ for $Co_{10}Zn_{10}$ and $Co_9Zn_9Mn_2$. This energy scale, which ultimately protects the metastable skyrmion state against decay, is much larger than the ferromagnetic exchange interaction (several 100 K), and thus attributed to the topological nature of the skyrmion with a large diameter (∼100 nm) that involves a great number of spins.

The coefficient of relaxation time τ_0 is inversely correlated to the critical cooling rate [67] required for quenching the SkX phase to lower temperatures. Since the obtained value of τ_0 in Co-Zn-Mn alloys is the order of a minute, the conventionally slow cooling rate ($dT/dt \sim -1$ K/min) is thus sufficient to quench the SkX phase. This is quite different from the value of $\tau_0 \sim 10^{-4}$ s in MnSi [64], where an ultrarapid cooling rate ($dT/dt \sim -100$ K/s) is necessary to quench the SkX phase. The large difference in τ_0 between the two systems is probably attributed to randomness in the system. In the case of Co-Zn-Mn alloys, there are random site occupancies in the crystal structure; the 8*c* site is randomly occupied by Co and Mn, and the 12*d* site is occupied by Co, Zn, and Mn [27–30]. This gives rise to "weak pinning" in the terminology of density wave physics [68], which may play an important role in the robust metastability of the skyrmion.

From a microscopic viewpoint, the destruction of metastable skyrmions in the bulk takes place through the creation of a pair of Bloch points (or equivalently an emergent magnetic monopole-antimonopole pair), from a singularity point of a skyrmion string, followed by their propagation [69,70], as schematically illustrated in Fig. 13(c). Coefficients a and τ_0 are roughly governed by the creation and the propagation processes of monopole-antimonopole pairs, respectively. In a clean system like MnSi, the monopole and antimonopole can easily move, which leads readily to skyrmion string destruction after the pair creation. In a dirty system like Co-Zn-Mn alloys, the movement of monopole and antimonopole is hindered by magnetic impurities or defects, and consequently τ_0 of the metastable skyrmion string is significantly increased. A similarly long-lived metastable SkX that is accessible by a moderate cooling rate has been reported in $Fe_{1-x}Co_xSi$ alloys [66,69,71], which may bear some resemblance to the present case. More recently, the increased lifetime of metastable SkX states has been observed also in Zn-doped Cu_2OSeO_3, where τ_0 in a Zn 2.5%-doped sample is 50 times larger than that in a nondoped sample while a remains unchanged [65]. In the present case of Co-Zn-Mn alloys, the good scaling of the τ vs T/T_c plot in Fig. 13(a) indicates that both a and τ_0 are almost independent of the Mn concentration. This is probably because $Co_{10}Zn_{10}$ already possesses substantial randomness in the site occupancy at the 12*d* site (2 Co and 10 Zn per unit cell), and thus the attempt time τ_0 is already sufficiently long and not further increased by additional randomness due to the Mn substitution. Nevertheless,

Mn substitution expands the equilibrium SkX phase toward lower temperature as seen in Figs. 12(a)–12(c) and 13(a), and hence the relaxation time just below the equilibrium SkX phase becomes longer. It is also interesting to note that the equilibrium skyrmion phase is expanded by static magnetic disorder while thermal fluctuation is considered to be important for the stability of the equilibrium phase close to T_c.

IV. CONCLUSION

In this study, to provide the perspective on the chiral magnetism in β-Mn-type Co-Zn-Mn alloys with bulk Dzyaloshinskii-Moriya interaction (DMI), we have performed magnetization, ac susceptibility, and small-angle neutron scattering measurements on single-crystal samples of $(Co_{0.5}Zn_{0.5})_{20-x}Mn_x$ with $x = 0$, 2, 4, and 6. The Mn-free end member $Co_{10}Zn_{10}$ exhibits a helimagnetic ground state (periodicity $\lambda \sim 156$ nm) below the transition temperature $T_c \sim 414$ K, where the helical propagation vector $\boldsymbol{q}$ is aligned with $\langle 111 \rangle$ at low temperatures (Fig. 5). Upon applying magnetic fields, $Co_{10}Zn_{10}$ exhibits an equilibrium SkX phase above 400 K in a narrow temperature and magnetic field region (Fig. 4), which is quenched down to lower temperatures as a metastable state by a conventionally slow field-cooling (Fig. 6). The lifetime of the metastable SkX is extremely long, being practically infinite below 380 K (Figs. 12 and 13). The metastable SkX state is highly robust and persists over the whole temperature range below T_c and a wide magnetic field region, including room temperature and zero field (Fig. 2). The lattice of metastable skyrmions distorts and transforms from a conventional triangular one to a rhombic one at low temperatures and low magnetic fields (Figs. 2 and 6).

As the partial substitution with Mn proceeds, T_c decreases and the preferred $\boldsymbol{q}$-vector orientation switches to $\langle 100 \rangle$. The saturation magnetization is the largest for $Co_9Zn_9Mn_2$ (Table I). At low temperatures, the helical q value significantly increases, or equivalently λ significantly decreases, below $T_H \sim 50$ K for $Co_9Zn_9Mn_2$ and below $T_H \sim 120$ K for $Co_8Zn_8Mn_4$ and $Co_7Zn_7Mn_6$ (Fig. 3). In $Co_7Zn_7Mn_6$, the helical state is severely disordered at low temperatures. Upon further decreasing temperature, a reentrant spin-glass transition occurs at $T_g \sim 10$ K for $Co_8Zn_8Mn_4$ and $T_g \sim 30$ K for $Co_7Zn_7Mn_6$ while such a transition is not observed for $Co_{10}Zn_{10}$ and $Co_9Zn_9Mn_2$ down to 2 K (Figs. 1 and 3). In common with $Co_{10}Zn_{10}$, a long-lived metastable SkX state is realized in the Mn-doped materials by a moderate FC through the equilibrium SkX phase, and persists over a wide temperature and field region. On the other hand, the lattice form of the metastable SkX changes to a square one at low temperatures (Figs. 2, 7, 8, and 9). While the triangular SkX is dictated by the applied field with $\boldsymbol{q}$-vectors $\perp H$, the square SkX is governed by the magnetocrystalline anisotropy that favors $\boldsymbol{q}$-vectors $\parallel \langle 100 \rangle$ regardless of the applied field direction (Figs. 7 and 8). During the transition to the square lattice, the periodicity of the SkX significantly shrinks below T_H similar to the helical periodicity in zero-field cooling (Fig. 3).

From these results, we conclude the following: The helical and skyrmion states in Co-Zn-Mn alloys are basically formed by ferromagnetic Co spins in the presence of the DMI. While Co and Mn are ferromagnetically coupled at least in the low Mn concentrations, antiferromagnetic Mn-Mn correlations become increasingly significant at higher Mn concentrations and start to develop at higher temperatures. As the temperature is lowered, the development of antiferromagnetic Mn-Mn correlation leads to a disordering of the helical state, a simultaneous decrease of the helical pitch, before ultimately undergoing a spin-freezing transition at very low temperatures. The robust metastability of skyrmions is attributed to the topological protection due to the large number of Co spins involved, as well as the weak pinning from the magnetic disorder. The structural transformations between a metastable triangular SkX and either a rhombic one or a square one are driven by a decrease in the distance between the skyrmions under the influence of the magnetocrystalline anisotropy that favors $\boldsymbol{q} \parallel \langle 111 \rangle$ and $\boldsymbol{q} \parallel \langle 100 \rangle$ in undoped and Mn-doped compounds, respectively. These findings unveil a complex interplay between chiral magnetism and frustrated Mn spins that is also greatly affected by magnetic disorder and anisotropy, and provide a significant understanding of the topological phases and properties in this class of β-Mn-type chiral magnets.

The data sets for the SANS experiments done on D33 at the ILL are available through the ILL data portal [72].

ACKNOWLEDGMENTS

We are grateful to T. Arima, T. Nakajima, D. Morikawa, X. Z. Yu, L. C. Peng, and N. Nagaosa for fruitful discussions. We thank M. Bartkowiak for support of SANS experiments above room temperature at Paul Scherrer Institute (PSI), Switzerland. This work was supported by JSPS Grant-in-Aids for Scientific Research (Grants No. 24224009 and No. 17K18355), JST CREST (Grant No. JPMJCR1874), the Swiss National Science Foundation (SNSF) Sinergia network "NanoSkyrmionics" (Grant No. CRSII5_171003), the SNSF Projects No. 200021_153451, No. 200021_188707, and No. 166298, and the European Research Council project CONQUEST.

[1] A. N. Bogdanov and D. A. Yablonskii, Zh. Eksp. Teor. Fiz. **95**, 178 (1989) [Sov. Phys. JETP **68**, 101 (1989)].

[2] N. Nagaosa and Y. Tokura, Nat. Nanotechnol. **8**, 899 (2013).

[3] S. Mühlbauer, B. Binz, F. Jonietz, C. Pfleiderer, A. Rosch, A. Neubauer, R. Georgii, and P. Böni, Science **323**, 915 (2009).

[4] X. Z. Yu, Y. Onose, N. Kanazawa, J. H. Park, J. H. Han, Y. Matsui, N. Nagaosa, and Y. Tokura, Nature (London) **465**, 901 (2010).

[5] F. Jonietz, S. Muhlbauer, C. Pfleiderer, A. Neubauer, W. Münzer, A. Bauer, T. Adams, R. Georgii, P. Böni, R. A. Duine, K. Everschor, M. Garst, and A. Rosch, Science **330**, 1648 (2010).

[6] X. Z. Yu, N. Kanazawa, W. Z. Zhang, T. Nagai, T. Hara, K. Kimoto, Y. Matsui, Y. Onose, and Y. Tokura, Nat. Commun. **3**, 988 (2012).

[7] J. Iwasaki, M. Mochizuki, and N. Nagaosa, Nat. Nanotechnol. **8**, 742 (2013).

[8] S. Heinze, K. von Bergmann, M. Menzel, J. Brede, A. Kubetzka, R. Wiesendanger, G. Bihlmayer, and S. Blügel, Nat. Phys. **7**, 713 (2011).

[9] N. Romming, C. Hanneken, M. Menzel, J. E. Bickel, B. Wolter, K. Bergmann, A. Kubetzka, and R. Wiesendanger, Science **341**, 636 (2013).

[10] J. Matsuno, N. Ogawa, K. Yasuda, F. Kagawa, W. Koshibae, N. Nagaosa, Y. Tokura, and M. Kawasaki, Sci. Adv. **2**, e1600304 (2016).

[11] S. Woo, K. Litzius, B. Krüger, M.-Y. Im, L. Caretta, K. Richter, M. Mann, A. Krone, R. Reeve, M. Weigand, P. Agrawal, P. Ischer, M. Kläui, G. S. D. Beach, I. Lemesh, and M.-A. Mawass, Nat. Mater. **15**, 501 (2016).

[12] A. Soumyanarayanan, M. Raju, A. L. G. Oyarce, A. K. C. Tan, M.-Y. Im, A. P. Petrovic, P. Ho, K. H. Khoo, M. Tran, C. K. Gan, F. Ernult, and C. Panagopoulos, Nat. Mater. **16**, 898 (2017).

[13] X. Z. Yu, N. Kanazawa, Y. Onose, K. Kimoto, W. Z. Zhang, S. Ishiwata, Y. Matsui, and Y. Tokura, Nat. Mater. **10**, 106 (2011).

[14] S. Seki, X. Z. Yu, S. Ishiwata, and Y. Tokura, Science **336**, 198 (2012).

[15] Y. Tokunaga, X. Z. Yu, J. S. White, H. M. Rønnow, D. Morikawa, Y. Taguchi, and Y. Tokura, Nat. Commun. **6**, 7638 (2015).

[16] W. Li, C. Jin, R. Che, W. Wei, L. Lin, L. Zhang, H. Du, M. Tian, and J. Zang, Phys. Rev. B **93**, 060409(R) (2016).

[17] I. Kézsmárki, S. Bordács, P. Milde, E. Neuber, L. M. Eng, J. S. White, H. M. Rønnow, C. D. Dewhurst, M. Mochizuki, K. Yanai, H. D. Ehlers, V. Tsurkan, and A. Loidl, Nat. Mater. **14**, 1116 (2015).

[18] T. Kurumaji, T. Nakajima, V. Ukleev, A. Feoktystov, T.-h. Arima, K. Kakurai, and Y. Tokura, Phys. Rev. Lett. **119**, 237201 (2017).

[19] A. K. Nayak, V. Kumar, T. Ma, P. Werner, E. Pippel, R. Sahoo, F. Damay, U. K. Rosler, C. Felser, and S. S. P. Parkin, Nature (London) **548**, 561 (2017).

[20] X. Z. Yu, Y. Tokunaga, Y. Kaneko, W. Z. Zhang, K. Kimoto, Y. Matsui, Y. Taguchi, and Y. Tokura, Nat. Commun. **5**, 3198 (2014).

[21] W. Wang, Y. Zhang, G. Xu, L. Peng, B. Ding, Y. Wang, Z. Hou, X. Zhang, X. Li, E. Liu, S. Wang, J. Cai, F. Wang, J. Li, F. Hu, G. Wu, B. Shen, and X.-X. Zhang, Adv. Mater. **28**, 6887 (2016).

[22] Z. Hou, W. Ren, B. Ding, G. Xu, Y. Wang, B. Yang, Y. Zhang, E. Liu, F. Xu, W. Wang, G. Wu, X. Zhang, B. Shen, and Z. Zhang, Adv. Mater. **29**, 1701144 (2017).

[23] R. Takagi, X. Z. Yu, J. S. White, K. Shibata, Y. Kaneko, G. Tatara, H. M. Rønnow, Y. Tokura, and S. Seki, Phys. Rev. Lett. **120**, 037203 (2018).

[24] M. Kakihana, D. Aoki, A. Nakamura, F. Honda, M. Nakashima, Y. Amako, S. Nakamura, T. Sakakibara, M. Hedo, T. Nakama, and Y. Ōnuki, J. Phys. Soc. Jpn. **87**, 023701 (2018).

[25] T. Kurumaji, T. Nakajima, M. Hirschberger, A. Kikkawa, Y. Yamasaki, H. Sagayama, H. Nakao, Y. Taguchi, T. Arima, and Y. Tokura, Science **365**, 914 (2019).

[26] M. Hirschberger, T. Nakajima, S. Gao, L. Peng, A. Kikkawa, T. Kurumaji, M. Kriener, Y. Yamasaki, H. Sagayama, H. Nakao, K. Ohishi, K. Kakurai, Y. Taguchi, X. Z. Yu, T. Arima, and Y. Tokura, Nat. Commun. **10**, 5831 (2019).

[27] T. Hori, H. Shiraish, and Y. Ishii, J. Magn. Magn. Mater. **310**, 1820 (2007).

[28] W. Xie, S. Thimmaiah, J. Lamsal, J. Liu, T. W. Heitmann, D. Quirinale, A. I. Goldman, V. Pecharsky, and G. J. Miller, Inorg. Chem. **52**, 9399 (2013).

[29] J. D. Bocarsly, C. Heikes, C. M. Brown, S. D. Wilson, and R. Seshadri, Phys. Rev. Mater. **3**, 014402 (2019).

[30] T. Nakajima, K. Karube, Y. Ishikawa, M. Yonemura, N. Reynolds, J. S. White, H. M. Rønnow, A. Kikkawa, Y. Tokunaga, Y. Taguchi, Y. Tokura, and T. Arima, Phys. Rev. B **100**, 064407 (2019).

[31] K. Karube, J. S. White, D. Morikawa, C. D. Dewhurst, R. Cubitt, A. Kikkawa, X. Z. Yu, Y. Tokunaga, T. Arima, H. M. Rønnow, Y. Tokura, and Y. Taguchi, Sci. Adv. **4**, eaar7043 (2018).

[32] R. Takagi, D. Morikawa, K. Karube, N. Kanazawa, K. Shibata, G. Tatara, Y. Tokunaga, T. Arima, Y. Taguchi, Y. Tokura, and S. Seki, Phys. Rev. B **95**, 220406(R) (2017).

[33] K. Karube, K. Shibata, J. S. White, T. Koretsune, X. Z. Yu, Y. Tokunaga, H. M. Rønnow, R. Arita, T. Arima, Y. Tokura, and Y. Taguchi, Phys. Rev. B **98**, 155120 (2018).

[34] K. Karube, J. S. White, N. Reynolds, J. L. Gavilano, H. Oike, A. Kikkawa, F. Kagawa, Y. Tokunaga, H. M. Rønnow, Y. Tokura, and Y. Taguchi, Nat. Mater. **15**, 1237 (2016).

[35] As explained in Sec. III F 2, there are two possibilities for the observed double-$\boldsymbol{q}$ state with increased q values: one is a coexistence of the square lattice of skyrmions and the helical state [Fig. 1(f)], and the other is elongated-skyrmion state on the square lattice [Fig. 1(g)]. Hereafter, we refer to the double-$\boldsymbol{q}$ state as "square lattice of skyrmions (or square SkX)" for the purpose of simplicity throughout the paper.

[36] K. Karube, J. S. White, D. Morikawa, M. Bartkowiak, A. Kikkawa, Y. Tokunaga, T. Arima, H. M. Rønnow, Y. Tokura, and Y. Taguchi, Phys. Rev. Mater. **1**, 074405 (2017).

[37] D. Morikawa, X. Z. Yu, K. Karube, Y. Tokunaga, Y. Taguchi, T. Arima, and Y. Tokura, Nano Lett. **17**, 1637 (2017).

[38] T. Nagase, M. Komatsu, Y. G. So, T. Ishida, H. Yoshida, Y. Kawaguchi, Y. Tanaka, K. Saitoh, N. Ikarashi, M. Kuwahara, and M. Nagao, Phys. Rev. Lett. **123**, 137203 (2019).

[39] X. Z. Yu, W. Koshibae, Y. Tokunaga, K. Shibata, Y. Taguchi, N. Nagaosa, and Y. Tokura, Nature (London) **564**, 95 (2018).

[40] H. Nakamura, K. Yoshimoto, M. Shiga, M. Nishi, and K. Kakurai, J. Phys.: Condens. Matter **9**, 4701 (1997).

[41] J. R. Stewart, B. D. Rainford, R. S. Eccleston, and R. Cywinski, Phys. Rev. Lett. **89**, 186403 (2002).

[42] J. R. Stewart, K. H. Andersen, and R. Cywinski, Phys. Rev. B **78**, 014428 (2008).

[43] J. R. Stewart and R. Cywinski, J. Phys.: Condens. Matter **21**, 124216 (2009).

[44] J. R. Stewart, A. D. Hillier, J. M. Hillier, and R. Cywinski, Phys. Rev. B **82**, 144439 (2010).

[45] J. A. M. Paddison, J. R. Stewart, P. Manuel, P. Courtois, G. J. McIntyre, B. D. Rainford, and A. L. Goodwin, Phys. Rev. Lett. **110**, 267207 (2013).

[46] It should be noted that the helimagnetic order formed by Co spins and the spin-glass state of frustrated Mn spins coexist. Therefore, it may also be called "embedded spin glass" as used in Ref. [51].

[47] B. R. Coles, B. V. B. Sarkissian, and R. H. Taylor, Philos. Mag. B **37**, 489 (1978).

[48] K. Motoya, S. M. Shapiro, and Y. Muraoka, Phys. Rev. B **28**, 6183 (1983).

[49] H. Maletta, G. Aeppli, and S. M. Shapiro, J. Magn. Magn. Mater. **31**, 1367 (1983).

[50] N. Hanasaki, K. Watanabe, T. Ohtsuka, I. Kézsmárki, S. Iguchi, S. Miyasaka, and Y. Tokura, Phys. Rev. Lett. **99**, 086401 (2007).

[51] J. O. Piatek, B. Dalla Piazza, N. Nikseresht, N. Tsyrulin, I. Živković, K. W. Krämer, M. Laver, K. Prokes, S. Mataš, N. B. Christensen, and H. M. Rønnow, Phys. Rev. B **88**, 014408 (2013).

[52] I. Mirebeau, N. Martin, M. Deutsch, L. J. Bannenberg, C. Pappas, G. Chaboussant, R. Cubitt, C. Decorse, and A. O. Leonov, Phys. Rev. B **98**, 014420 (2018).

[53] H. Yoshizawa, S. Mitsuda, H. Aruga, and A. Ito, J. Phys. Soc. Jpn. **58**, 1416 (1989).

[54] C. J. Leavey, J. R. Stewart, B. D. Rainford, and A. D. Hillier, J. Phys.: Condens. Matter **19**, 145288 (2007).

[55] T. Sato and K. Morita, J. Phys.: Condens. Matter **11**, 4231 (1999).

[56] In Ref. [31] we reported for $Co_7Zn_7Mn_6$ that the real part of the ac susceptibility exhibits a drop, the imaginary part a peak at $T_g \sim$ 30 K, and the frequency-dependent T_g increases (29 K $\rightarrow$ 34 K) as the ac frequency f is increased (0.1 Hz $\rightarrow$ 1000 Hz). The frequency dependence of T_g satisfies a power law $f^{-1} = \tau_0[T_g(f)/T_g(0) - 1]^{-z\nu}$ [$\tau_0 = 5.3 \times 10^{-8}$ s, $T_g(0) = 24.6$ K, $z\nu = 10.7$]. The slow spin-flipping time $\tau_0 \sim 10^{-8}$ s is a typical value for reentrant spin glass [50]. A similar measurement for $Co_7Zn_7Mn_6$was also reported in Ref. [29].

[57] See Supplemental Material at http://link.aps.org/supplemental/10.1103/PhysRevB.102.064408 for additional data of magnetization, ac susceptibility, and small-angle neutron scattering in Co-Zn-Mn alloys.

[58] The asymmetric peak broadenings around the [−111] and [1−1−1] directions at 1.5 K are attributed to imperfect summations of SANS patterns along the rocking direction.

[59] Y. Togawa, T. Koyama, K. Takayanagi, S. Mori, Y. Kousaka, J. Akimitsu, S. Nishihara, K. Inoue, A. S. Ovchinnikov, and J. Kishine, Phys. Rev. Lett. **108**, 107202 (2012).

[60] On the basis of demagnetization coefficients in the rectangular-shaped sample and a magnetization value at 295 K, the extra tilt angle α of the effective magnetic field $H_{\rm eff}$ from the external field H was calculated to be $\alpha = 23^\circ$, showing a good agreement with the observed peak position of the rocking curve at 295 K.

[61] V. Ukleev, Y. Yamasaki, D. Morikawa, K. Karube, K. Shibata, Y. Tokunaga, Y. Okamura, K. Amemiya, M. Valvidares, H. Nakao, Y. Taguchi, Y. Tokura, and T. Arima, Phys. Rev. B **99**, 144408 (2019).

[62] S. D. Yi, S. Onoda, N. Nagaosa, and J. H. Han, Phys. Rev. B **80**, 054416 (2009).

[63] S.-Z. Lin, A. Saxena, and C. D. Batista, Phys. Rev. B **91**, 224407 (2015).

[64] H. Oike, A. Kikkawa, N. Kanazawa, Y. Taguchi, M. Kawasaki, Y. Tokura, and F. Kagawa, Nat. Phys. **12**, 62 (2016).

[65] M. T. Birch, R. Takagi, S. Seki, M. N. Wilson, F. Kagawa, A. Štefančič, G. Balakrishnan, R. Fan, P. Steadman, C. J. Ottley, M. Crisanti, R. Cubitt, T. Lancaster, Y. Tokura, and P. D. Hatton, Phys. Rev. B **100**, 014425 (2019).

[66] J. Wild, T. N. G. Meier, S. Pollath, M. Kronseder, A. Bauer, A. Chacon, M. Halder, M. Schowalter, A. Rosenauer, J. Zweck, J. Muller, A. Rosch, C. Pfleiderer, C. H. Back *et al.*, Sci. Adv. **3**, e1701704 (2017).

[67] F. Kagawa and H. Oike, Adv. Mater. **29**, 1601979 (2017).

[68] G. Grüner, Rev. Mod. Phys. **60**, 1129 (1988).

[69] P. Milde, D. Köhler, J. Seidel, L. M. Eng, A. Bauer, A. Chacon, J. Kindervater, S. Mühlbauer, C. Pfleiderer, S. Buhrandt, C. Schütte, and A. Rosch, Science **340**, 1076 (2013).

[70] F. Kagawa, H. Oike, W. Koshibae, A. Kikkawa, Y. Okamura, Y. Taguchi, N. Nagaosa, and Y. Tokura, Nat. Commun. **8**, 1332 (2017).

[71] W. Münzer, A. Neubauer, T. Adams, S. Mühlbauer, C. Franz, F. Jonietz, R. Georgii, P. Böni, B. Pedersen, M. Schmidt, A. Rosch, and C. Pfleiderer, Phys. Rev. B **81**, 041203(R) (2010).

[72] http://doi.ill.fr/10.5291/ILL-DATA.5-42-410 and http://doi.ill.fr/10.5291/ILL-DATA.5-42-443